Journal of Hydrology 663 (2025) 134223

Contents lists available at ScienceDirect

Journal of Hydrology

journal homepage: www.elsevier.com/locate/jhydrol

Research papers

Water vapor sorption behavior of shale organic matter with various types and maturation

Jiajun Fu [a,b], Ke Xu [c], Yeping Ji [d], Xuezhe Wang [a], Yiquan Ma [b], Mehdi Ostadhassan [a], Zhejun Pan [a], Duo Wang [a], Bo Liu [a], Yubing Ke [e,f], Mengdi Sun [a,b,c,*]

[a] State Key Laboratory of Continental Shale Oil, Northeast Petroleum University, Daqing 163318, China
[b] State Key Laboratory of Oil and Gas Reservoir Geology and Exploitation, Chengdu University of Technology, Chengdu 610059, China
[c] Department of Energy and Resources Engineering, Peking University, China
[d] CSIRO Energy, Perth, WA 6151, Australia
[e] Institute of High Energy Physics, Chinese Academy of Sciences (CAS), Beijing 100049, China
[f] Spallation Source Neutron Science Center, Dongguan 523803, China

ARTICLE INFO

This manuscript was handled by Huaming Guo, Editor-in-Chief, with the assistance of Mingjie Chen, Associate Editor

Keywords:
Maturity
Adsorption model
Pore surface property
Functional groups
Pore structure

ABSTRACT

To investigate the water vapor adsorption (WVA) behavior of shale organic matter (OM), we conducted a series of WVA experiments integrated with gas physisorption, Fourier transform infrared spectroscopy (FTIR), and small-angle neutron scattering (SANS) on six OM samples with varying types (I, II, and III) and maturities (R_o: 1.21–3.56 %). The adsorption process was analyzed using the Dent and Freundlich models. Results indicate that capillary condensation accounts for more than 50% of the total WVA capacity at RH 0.95. Layered adsorption is primarily governed by pore surface properties: Type III OM, contains carboxyl groups, exhibits the strongest adsorption strength, whereas overmature Type I OM, despite exhibiting rough pore surfaces and abundant adsorption sites, shows comparatively weak adsorption strength. Pore volume (PV) and specific surface area (SSA) provide the spatial basis for adsorption. Moreover, the presence of strongly hydrophilic functional groups (particularly carboxyl) and enhanced pore connectivity can extend the effective adsorption pore size range, further facilitating WVA. Among the OM types, Type I exhibits the greatest pore development and connectivity but lacks hydrophilic functional groups, while Type III shows the opposite characteristics. Maturity also exerts a significant influence on both pore structure and surface properties. These findings highlight the coupling effects of pore structure and surface properties in controlling WVA and fill the research gap into the adsorption behavior of shale OM with different types and maturities.

1. Introduction

Over the past two decades, shale oil and gas have emerged as vital components of the global energy mix, attracting widespread attention. The extensive use of hydraulic fracturing has introduced large volumes of aqueous fracturing fluids into shale reservoirs (Wang et al., 2025; Curtis, 2002), which significantly impairs the occurrence and migration of hydrocarbons. Substantial evidence indicates that water competes with methane for adsorption sites, leading to a reduction in methane adsorption by >50 % (Feng et al., 2024; Ma and Yu, 2022; Zhu et al., 2021; Gasparik et al., 2014; Ross and Marc Bustin, 2009). Moreover, the presence of water severely diminishes gas transport efficiency of gas recovery (Zhang et al., 2022; Charrière and Behra, 2010). Therefore, a comprehensive understanding of the water adsorption behavior of shale is essential for accurately evaluating and effectively developing shale oil and gas resources.

Water vapor adsorption (WVA) is widely recognized as a primary experimental approach for investigating the water adsorption behavior of shale (Dang et al., 2021; Li et al., 2021; Yang et al., 2020; Sang et al., 2019; Zolfaghari et al., 2017b). During WVA experiments, as relative humidity (RH) increases from low to high, the adsorption process transitions sequentially from monolayer adsorption to multilayer adsorption, and eventually to capillary condensation (Xie et al., 2023). Additionally, with increasing RH, water vapor progressively adsorbs and condenses within pores of increasing diameter (Yang et al., 2020; Zolfaghari et al., 2017b). Numerous studies have demonstrated that clay

---

[*] Corresponding author at: State Key Laboratory of Continental Shale Oil, Northeast Petroleum University, Daqing 163318, China.
E-mail address: sunmd@nepu.edu.cn (M. Sun).

https://doi.org/10.1016/j.jhydrol.2025.134223
Received 26 June 2025; Received in revised form 18 August 2025; Accepted 5 September 2025

minerals play a critical role in the WVA capacity of shale (Xie et al., 2023; Wang et al., 2019; Zolfaghari et al., 2017a). The high WVA capacity and strong hydrophilicity of clay minerals are attributed to their negatively charged surfaces and their ability to hydrate exchangeable cations (Xiong et al., 2023).

Unlike clay minerals, organic matter (OM), despite typically developing a large number of pores, exhibits highly complex and inconclusive water adsorption behavior. For instance, Zhu et al. (2021) reported that shale samples with higher total organic carbon (TOC) content showed lower WVA capacity. Similarly, some studies suggest that organic pores are generally water-free or possess weak WVA capacity (Xu et al., 2019; Zolfaghari et al., 2017b). In contrast, WVA experiments on Illinois Shales demonstrated that kerogen-rich samples exhibited substantial WVA capacity (Sang et al., 2019). Shen et al. (2019) also found a positive correlation between TOC and WVA capacity. However, these studies primarily focused on whole rock samples rather than isolated OM, making it difficult to accurately assess the intrinsic water adsorption behavior of OM itself.

However, only a limited number of studies have employed WVA to investigate OM isolated from shale (Xing et al., 2025; Ukaomah et al., 2023; Zhang et al., 2022; Zhu et al., 2021). Regarding the mechanisms of water adsorption, Ukaomah et al. (2023) proposed that OM adsorbs water molecules primarily through hydrophilic oxygen-containing functional groups. In contrast, Zhang et al. (2022) argued that hydrophobic OM can still provide adsorption sites via residual water and a small number of oxygen atoms within its structure. As for WVA capacity, overmature kerogen from the Qiongzhusi shale was found to exhibit significantly higher WVA capacity than the original rock (Xing et al., 2025). Similarly, Ukaomah et al. (2023) reported that the WVA capacity of isolated OM was several times greater than that of the corresponding whole rock. Conversely, Zhu et al. (2021) found that kerogen exhibited extremely weak WVA capacity, only 1/20 that of montmorillonite. It is well known that the complex and diverse compositions and thermal evolution histories of OM give rise to distinct physicochemical and structural properties (Liu et al., 2022; Katz and Arango, 2018; Curtis et al., 2012; Tissot and Welte, 1984), which may lead to variations in WVA behavior. Therefore, inconsistencies in previous findings likely stem from differences in OM type and maturity.

In this study, six OM samples representing different types (I, II, and III) and maturities from various regions were selected for WVA experiments. The functional group composition and pore structure of the samples were characterized using Fourier transform infrared spectroscopy (FTIR), gas physisorption, field emission-scanning electron microscopy (FE-SEM), and small-angle neutron scattering (SANS). The WVA processes were analyzed using the Dent and Freundlich models. The primary objective was to identify the key factors influencing WVA behavior of OM and to systematically evaluate the adsorption mechanisms and differences associated with OM type and thermal maturity. It is important to note that organic pores in OM can be broadly categorized into primary pores, which originate from biological structures, and secondary pores, which form during thermal evolution (Wu et al., 2020; Cardott and Curtis, 2018; Katz and Arango, 2018). Primary pores, typically ranging from hundreds of nanometers to tens of micrometers, contribute minimally to the overall shale pore system. In contrast, secondary nanoscale pores play a dominant role in determining the specific surface area (SSA) and pore volume (PV) of shale (Liu et al., 2022; Liu et al., 2017). Accordingly, this study focuses primarily on secondary organic pores.

2. Samples and methods

2.1. Sample and preparation

Six shale core samples were collected from China for this study, five from the Sichuan Basin and its surrounding areas, and one from the Ordos Basin (Fig. 1). These samples were derived from formations containing Type I OM from the Yanchang Formation (Xiao et al., 2021) and the Niutaitang Formation (Wang et al., 2024); Type II OM from the Longmaxi Formation (Liu et al., 2011) and the Wufeng Formation (Niu et al., 2024); and Type III OM from the Longtan Formation (Wu et al., 2020). Among them, YC1 and LT1 are argillaceous shale, LM1 is calcareous shale, while LM2, WF1, and NT1 are siliceous shale. The R_o values of the selected samples range from 1.21 % to 3.56 %. Table 1 provides exhaustive details concerning the samples.

Six shale samples were cut into small pieces of size about 8 mm × 8 mm × 3 mm for FE-SEM observation. Before investigating the OM samples (Fig. 2), it was necessary to isolate them from the crushed shale samples (80–100 mesh). The OM samples were extracted using a chemical extraction procedure applied to powdered shale (Zhang et al., 2020; Sun et al., 2018). First, the samples were soaked in distilled water for 2–4 h to allow full swelling, after which the water was removed. Second, 6 mol/L hydrochloric acid (HCl) and 40 % hydrofluoric acid (HF) were added to the samples and stirred thoroughly to remove carbonates. Third, the residue was treated with 6 mol/L HCl and arsenic-free zinc powder until no hydrogen sulfide (H_2S) gas was produced, ensuring the complete removal of pyrite. Fourth, OM was separated using heavy liquid separation with a shaker, followed by multiple rinses with distilled water to eliminate halide ions. Finally, the purified OM was stored at 5 °C for 6 h for preservation. To eliminate any remaining water, the separated OM samples were subsequently evaporated for

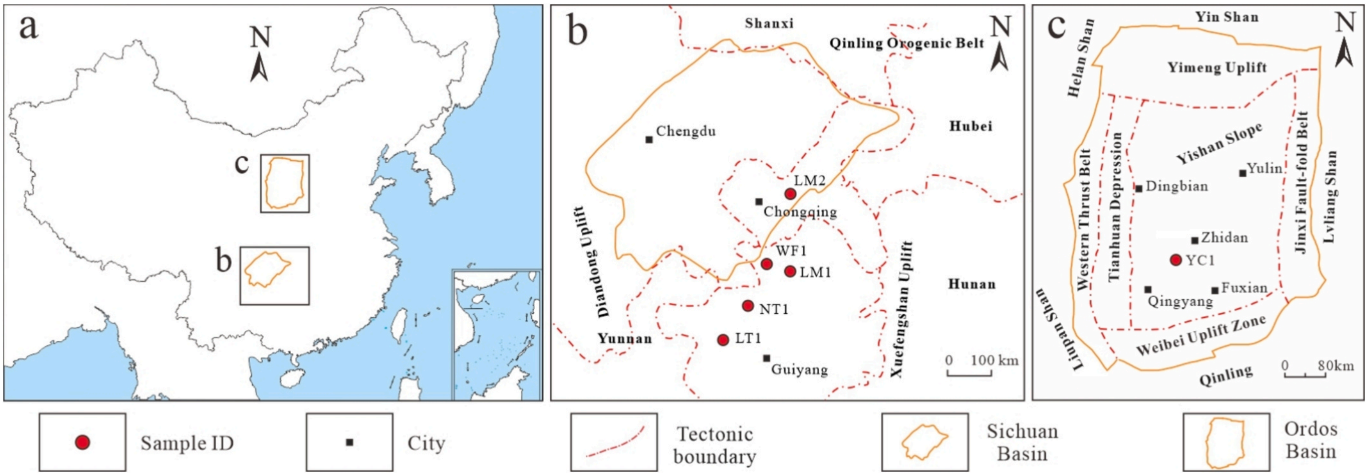

Fig. 1. (a) Location of Sichuan basin and Ordos basin in China (modified from Cui et al., 2024); (b) Location of samples in Sichuan basin and its periphery (modified from Tian et al., 2024); (c) Location of sample in Ordos basin (modified from Cui et al., 2024).

Table 1
Basic properties of shale samples.

Sample ID	Formation	Depth (m)	TOC (%)	R_o (%)	OM type	Quantitative analysis of whole-rock minerals (wt.%)					
						Quartz	Calcite	Dolomite	Plagioclase	Pyrite	Clays
YC1	Upper Triassic Yanchang	1607	4.21	1.21	I	25	0	1	4	1	66
LM1	Lower Silurian Longmaxi	670	7.58	2.12	II	30	28	5	10	5	21
LM2	Lower Silurian Longmaxi	2350	4.42	2.21	II	46	4	5	7	8	25
WF1	Upper Ordovician Wufeng	645	4.95	2.34	II	64	5	7	3	2	19
LT1	Upper Permian Longtan	937	3.41	2.52	III	31	0	0	3	6	60
NT1	Lower Cambrian Niutitang	927	11.6	3.56	I	74	1	2	2	4	16

Note: TOC = Total organic carbon. R_o = Vitrinite reflectance. OM = Organic matter.

Fig. 2. Photo of organic matter extracted from six shale samples.

more than 48 h at 60 ℃ in a vacuum oven. Following this, the dried OM samples were analyzed using FTIR, gas (N_2 and CO_2) physisorption, SANS, and WVA.

2.2. FE-SEM

Prior to imaging, a 10 nm thick covering of gold was sprayed onto the sample surfaces to improve conductivity after they were previously polished with an Ilion+ II (Model 697, Gatan, a broad beam ion milling system). Images were then collected with a FE-SEM (Zeiss Merlin) at a working distance of 2–4 mm and a voltage of 1 kV.

2.3. FTIR

Prior to the experiment, 0.2 g of dried OM was mixed with potassium bromide in a 1:100 ratio and ground in an agate mortar. The resulting mixture was then placed in a tablet compactor and pressed into a thin slice at a pressure of 10 MPa. The tablet was dried at 60 ℃ for 6 h before being analyzed using a Bruker Vertex 70 infrared spectrometer. Measurements were conducted at 25 ℃ and 50 % relative humidity. Spectra were recorded in the wavenumber range of 4000–650 cm^{-1} with a resolution of 4 cm^{-1}. The experiment was performed in transmission mode with 16 scans. Raw data were processed using OMNIC software and subsequently exported.

2.4. Gas physisorption

To prevent damage to the OM samples from high temperatures and to remove any water and residual volatiles, the samples were degassed at 80 ℃ for 12 h under vacuum prior to measurement using a Micromeritics 2460 apparatus. N_2 adsorption isotherms were recorded at −196 ℃ in the relative pressure range of P/P_0 from 0.009 to 0.995, while the desorption isotherm was measured from $P/P_0 = 0.995$ to 0.2. The Brunauer-Emmett-Teller (BET) and Barrett-Joyner-Halenda (BJH) theories were applied to determine the N_2 SSA and pore size distribution. CO_2 adsorption experiments were conducted at 0 ℃, with data recorded for P/P_0 ranging from 0.00001 to 0.03. The CO_2 pore structure data was calculated using Density Functional Theory (DFT).

2.5. SANS

SANS is a non-destructive radiation-based probing technique. After collimation, the incident neutron beam is directed onto the sample. Elastic scattering arises from the contrast in scattering length density (SLD) between the pores and the solid components of the sample, and the scattered neutrons are subsequently recorded by a detector (Fig. 3). After 48 h of drying at 60 ℃, the OM samples were put in quartz cells to be tested to offer raw 2D data. The data were corrected using background measurements from the empty cell and a quartz sand test of the same size as the sample. For 2D data without anisotropy, sector integration is sufficient to extract representative 1D data, which were subsequently analyzed using the polydisperse size distribution model (PDSM) model. The pore structure data was calculated by the IRENA plug-in of Igor Pro, in combination with the SLD of sample. According to the relationship between SLD and maturity (Ruppert et al., 2013), the SLD of 6 OM samples were calculated (Table 2).

The PDSM model is based on a two-phase system consisting of pores and a solid matrix. It assumes that the pore shape is spherical, and the pore structure is evaluated using the following equation:

$$I(q) = (\rho_1 - \rho_2)^2 \sum P(q,r)^2 F(r) V(r)^2 N \Delta r \tag{1}$$

where ρ_1 and ρ_2 represent the SLD values of the solid matrix and pore space, respectively, r expresses the radius of the pore, $P(q,r)$ stands for the shape coefficient of the pore with radius r, $F(r)$ is the pore size distribution function, $V(r)$ signifies the volume of the pore with radius r, and N is the number of pores.

The scattering intensity $I(q)$ corresponding to different scattering vectors q is measured experimentally, and pore structure data are obtained through model fitting. Here, $q = 4\pi \sin\theta/\lambda$, where λ is the wavelength of the incident neutron and θ is half of the scattering angle between the scattered and incident neutrons. According to Radliński et al. (2000), the formula $r = 2.5/q$ characterizes the connection between q and the pore radius (r). Thus, the q range reflects the range of

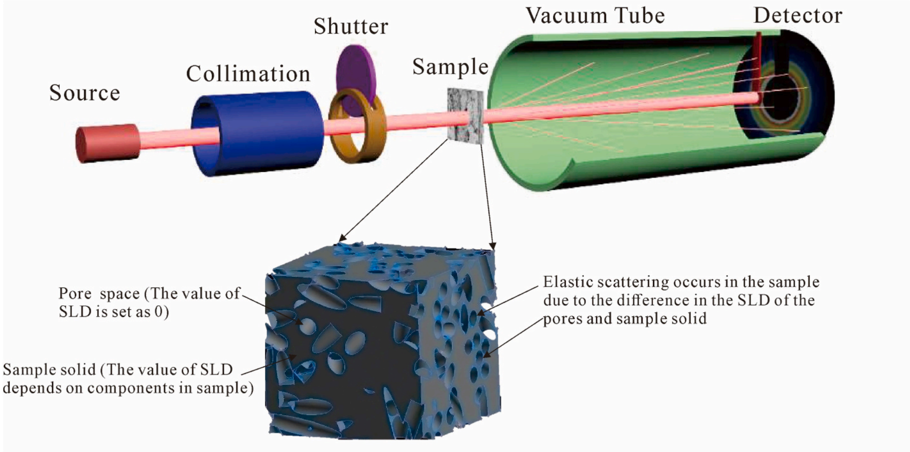

Fig. 3. Principle of SANS experiment (modified from Sun et al., 2020).

Table 2

Pore structure parameters obtained from SANS experiments.

Sample ID	SANS SLD ($\times 10^{10}$cm^{-2})	SANS flat background (cm^{-1})	PDSM Porosity (%)	Fractal dimension
YC1	2.53	0.479	21.21	Dm 2.961
LM1	3.07	0.148	12.45	Ds 2.601
LM2	3.13	0.099	19.21	Ds 2.795
WF1	3.20	0.105	13.05	Ds 2.718
LT1	3.31	0.258	7.11	Ds 2.261
NT1	3.94	0.057	9.91	Ds 2.902

Note: SLD = Scattering length density. Dm = Mass fractal dimension. Ds = Surface fractal dimension.

experimentally tested pore radius. SANS experiments are typically conducted by varying the sample-to-detector distance and using different neutron wavelengths to achieve different q ranges. In this study, OM samples completed SANS test at the China Spallation Neutron Source. A constant sample-to-detector distance of 4 m was employed in the experiment, achieving a q range of 0.0046–0.68 Å^{-1} by varying the incident neutron wavelength (λ = 1–10 Å).

2.6. WVA

WVA experiments were carried out using the dynamic vapor sorption (DVS) method. OM samples were tested at 25 ℃ over a RH range of 0.002–0.95 using a Quantachrome Aquadyne DVS-2 Water Sorption Instrument. This instrument offers precise temperature and humidity control, along with accurate mass measurements. The sample chamber humidity is regulated by mixing dry and moist nitrogen, with a resolution of 1 %. The temperature control system has a resolution of 0.1 °C, and the microbalance used for measuring sample mass has a resolution of 0.1 μg. Prior to the experiment, the sample chamber was purged for more than 10 min to ensure dryness, and the microbalance was calibrated. For each measurement, a sample of approximately 20 mg OM was loaded into the sample chamber. As the sample mass stabilizes at each humidity level, the system progressively adjusts the humidity to the next stage.

Adsorption models are essential for understanding the WVA behavior in greater detail. The Dent model (Dent, 1977), an extension of the BET model (Brunauer et al., 1938), not only fits the adsorption data of shale well, but also divides the procedure into primary and secondary adsorption. Primary sites on the pore surface exhibit a strong binding affinity for water molecules, while secondary sites include hydrophobic areas and multilayer adsorption sites beyond the monolayer adsorption. Unlike the BET model, which is only applicable in the RH range of 0.05–0.35, the Dent model can be used across the entire experimental testing RH range. The equation for the Dent model is as follows (Dent, 1977):

$$Q = \frac{q_m K_1 RH}{(1 - K_2 RH)(1 - K_2 RH + K_1 RH)} \tag{2}$$

$$Q_1 = \frac{q_m K_1 RH}{1 - K_2 RH + K_1 RH} \tag{3}$$

$$Q_2 = \frac{q_m K_1 K_2 RH^2}{(1 - K_2 RH)(1 - K_2 RH + K_1 RH)} \tag{4}$$

In this model, Q represents the total WVA capacity (mg/g), and q_m represents the maximum WVA capacity via monolayer adsorption (mg/g), corresponding to the saturated WVA capacity at primary adsorption sites. K_1 is a dimensionless constant reflecting the adsorption strength at primary sites, which indicates the interaction intensity between the pore surfaces and water molecules. K_2 is another dimensionless constant that represents the adsorption strength at secondary sites. Note that K_1 and K_2 only represent the relative adsorption strength and do not correspond to absolute values. Q_1 and Q_2 represent the WVA capacity of primary and secondary adsorption, respectively (mg/g).

Additionally, the Freundlich model, an empirical adsorption model derived from statistical mechanics and thermodynamics, can identify distinct adsorption processes. The linear form of the Freundlich model is given by:

$$\ln Q = \ln k + \frac{1}{n} \ln RH \tag{5}$$

where n is a dimensionless constant indicating the adsorption strength of OM for water molecules, without reflecting an absolute physical value. The constant k represents the fitted WVA capacity (mg/g) derived from empirical modeling and does not correspond to the actual measurable capacity.

3. Results

3.1. FTIR

Fig. 4 presents the FTIR transmittance spectra of the six OM samples. The main absorption peaks observed include: the O–H stretching vibration of alcohol/phenol (3200–3700 cm^{-1}), the O–H stretching vibration of carboxyl groups (2500–3200 cm^{-1}, broad and strong), the C–H stretching vibration of aliphatic hydrocarbons (2850–3000 cm^{-1}), the C=C skeletal vibration of aromatic hydrocarbons (1450–1600 cm^{-1}), the C–H bending vibration of aliphatic hydrocarbons

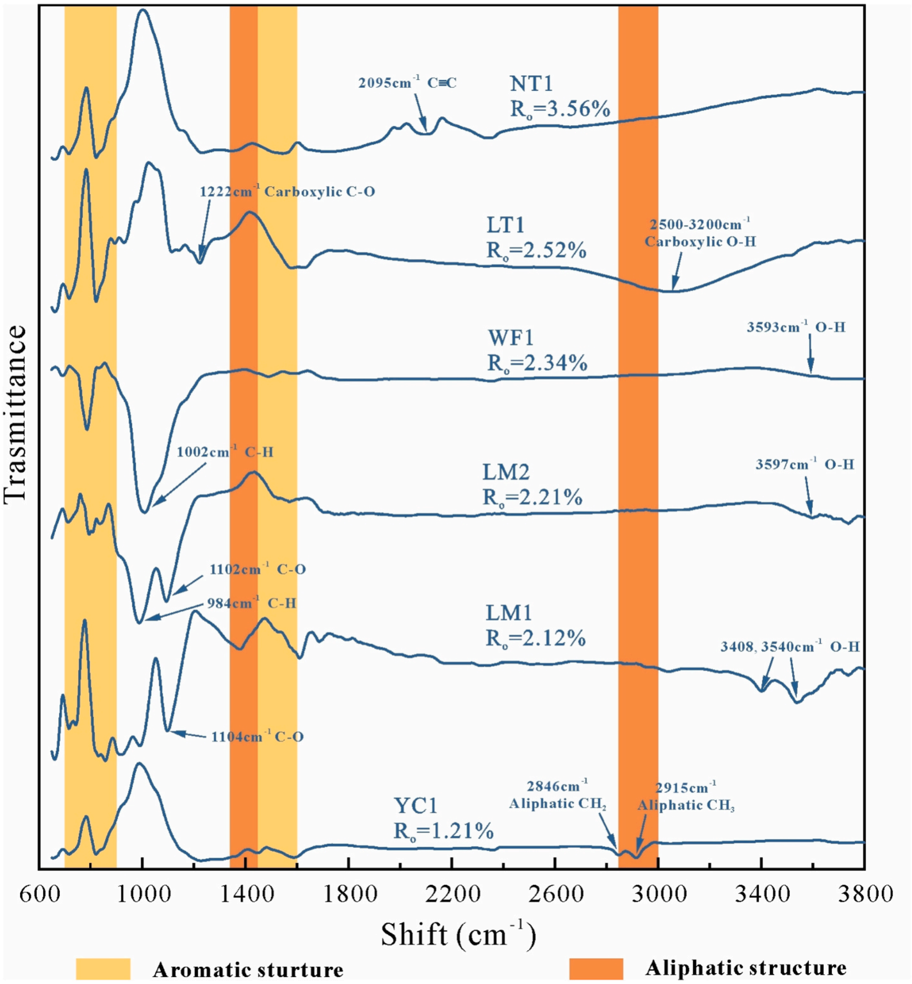

Fig. 4. FTIR spectra of OM samples.

(1350–1450 cm^{-1}), the C–O stretching vibration (1000–1300 cm^{-1}), and the out-of-plane C–H bending vibration of aromatic hydrocarbons (700–900 cm^{-1}). The positions and intensities of these characteristic peaks vary significantly among the samples due to differences in OM type and thermal maturity. The YC1 sample primarily exhibits characteristic peaks in the regions corresponding to aliphatic and aromatic structures, with distinct peaks at 2846 cm^{-1} and 2915 cm^{-1}, representing $–CH_2$ and $–CH_3$, respectively, which are absent in other samples. Since NT1 is also a Type I OM, its FTIR spectrum is similar to that of YC1. However, YC1 no longer exhibits C–H stretching vibrations characteristic of aliphatic structures (2850–3000 cm^{-1}). Additionally, neither YC1 nor NT1 exhibit O–H stretching vibrations characteristic of hydroxyl groups (3200–3700 cm^{-1}), indicating the absence of hydroxyl groups. In contrast, the LT1, LM1, LM2, and WF1 samples show characteristic peaks not only in the aromatic structures but also in oxygen-containing functional groups such as O–H and C–O, distinguishing them from YC1 and NT1. LT1 exhibits a broad peak for the O–H stretching vibration of the carboxyl groups (2500–3200 cm^{-1}) and a peak for the C–O stretching vibration of the carboxyl groups (1222 cm^{-1}), indicating that LT1 contains carboxyl groups. LM1, LM2, and WF1 exhibit hydroxyl O–H stretching vibration peaks (3200–3700 cm^{-1}) and C–O stretching vibration peaks (1000–1300 cm^{-1}) to varying degrees, indicating the presence of hydroxyl groups.

3.2. *Gas physisorption*

According to the IUPAC classification (Sing, 1985), all N_2 adsorption isotherms fall into type II, indicating the existence of multilayer adsorption (Fig. 5). Adsorption increases rapidly at low relative pressures ($P/P_0 < 0.1$), indicating that nitrogen fills the micropores. When P/P_0 reaches 0.1, the isotherm demonstrates an inflection point, marking the completion of monolayer adsorption and the onset of multilayer adsorption. As P/P_0 exceeds 0.9, the adsorption sharply increases, indicating that the samples primarily contain micropores and mesopores (diameters less than 50 nm), with fewer macropores (diameters greater than 50 nm). Hysteresis loops are observed in all the N_2 adsorption/desorption curves (Fig. 5). The NT1 sample exhibits a Type H3 loop, while the other five samples exhibit a mixed morphology between Type H2 and H3 loops. Type H2 and H3 represent slit-shaped and inkbottle-shaped pores, respectively. In LM1, LM2, WF1, and LT1, the hysteresis loops do not close at lower P/P_0 values. This phenomenon, also reported in previous studies, may result from OM swelling during the adsorption process, incomplete desorption of N_2, or an irreversible adsorption process (Chen et al., 2018). The CO_2 adsorption isotherms explain that the volume of adsorbed gas in the OM samples increases with the increase of relative pressure (Fig. 6). Unlike nitrogen adsorption, the isotherm of LT1 for carbon dioxide is significantly higher than that of other samples, indicating the presence of more micropores. In addition, the curves of YC1 and NT1 show similar morphological characteristics, while LM1, LM2, and WF1 exhibit a different morphology, which may be related to the type of OM.

As shown in Table 3, the N_2 pore volume (PV) of the OM samples range from 0.0296 to 0.2682 cm^3/g, while CO_2 PV range from 0.0016 to 0.012 cm^3/g. N_2 derived PV values are significantly higher than those

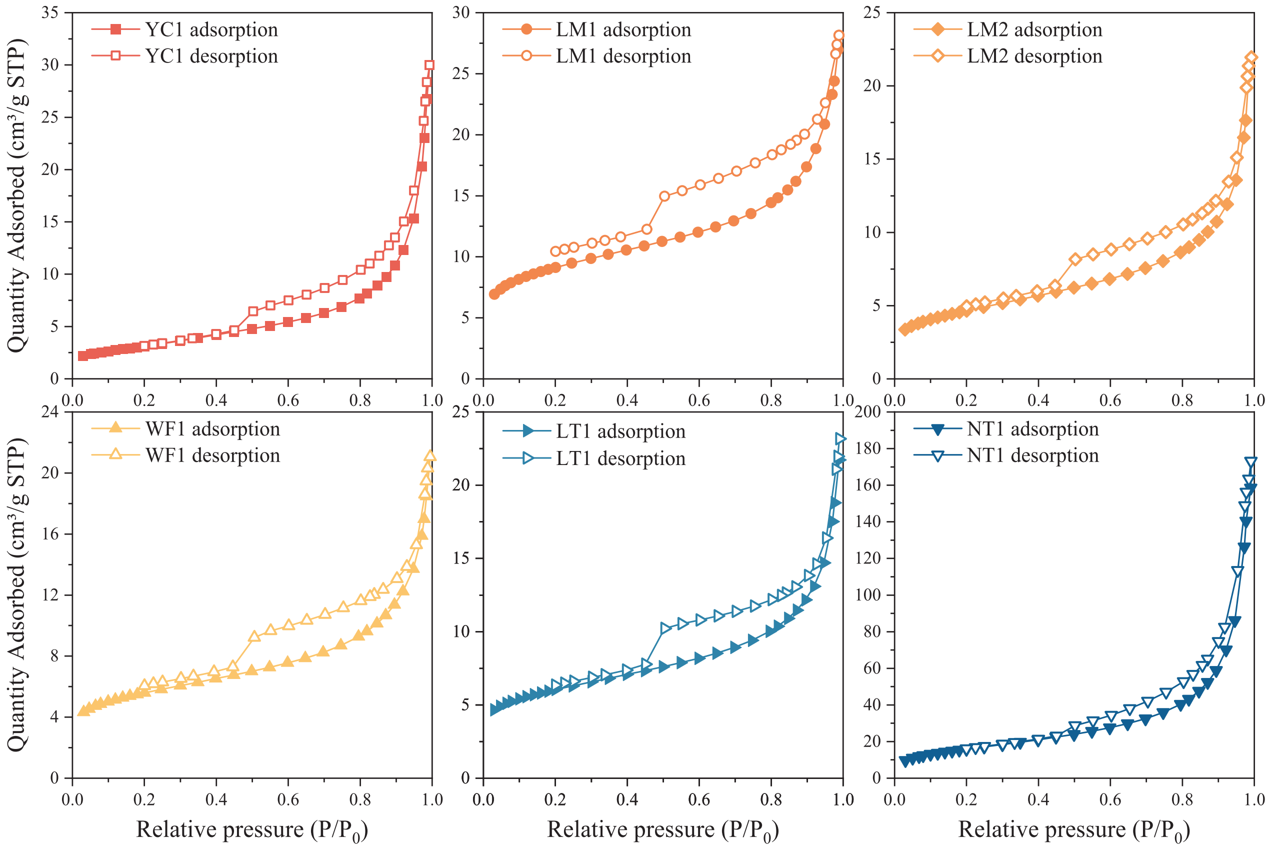

Fig. 5. N_2 adsorption/desorption isotherms obtained from OM samples.

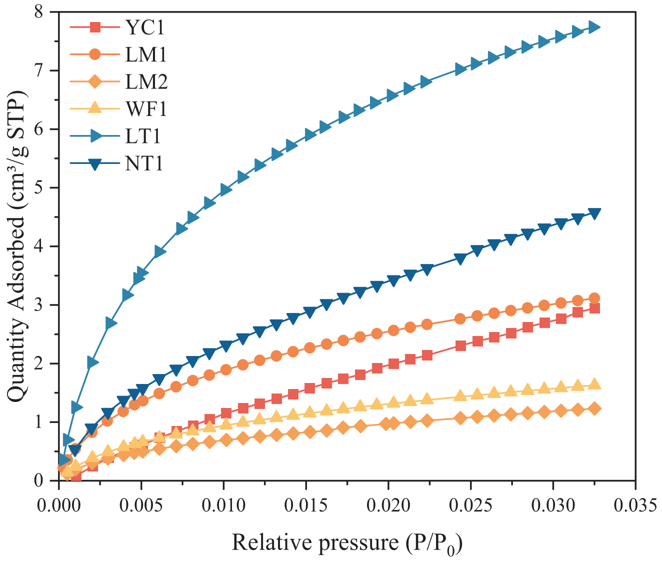

Fig. 6. CO_2 adsorption isotherms obtained from OM samples.

from CO_2 measurements. This implies that mesopores and macropores are more developed than micropores in the OM samples. In contrast to the other samples, which range from 0.0317 to 0.0484 cm^3/g, NT1 has a significantly higher total PV (0.2724 cm^3/g). With the exception of LT1, the N_2 SSA of all samples exceeded their CO_2 SSA, suggesting that LT1 has a greater proportion of developed micropores. The N_2 and CO_2 SSA of the samples vary from 11.32 to 58.14 m^2/g and from 5.17 to 40.76 m^2/g, respectively, while the total SSA range is from 16.49 to 73.09 m^2/g.

Table 3
Pore structure parameters of OM samples from N_2 and CO_2 physisorption.

Sample ID	YC1	LM1	LM2	WF1	LT1	NT1
N_2 V_{BJH} (cm^3/g)	0.0467	0.0383	0.0332	0.0296	0.0328	0.2682
CO_2 V_{DFT} (cm^3/g)	0.0017	0.0042	0.0016	0.0021	0.0120	0.0042
V_g (cm^3/g)	0.0484	0.0425	0.0348	0.0317	0.0448	0.2724
N_2 S_{BET} (m^2/g)	11.32	30.32	16.33	19.17	20.75	58.14
CO_2 S_{DFT} (m^2/g)	5.17	14.64	5.40	7.18	40.76	14.95
S_g (m^2/g)	16.49	44.96	21.73	26.35	61.51	73.09

Note: N_2 V_{BJH} = The PV calculated by N_2 physisorption using the BJH theory. CO_2 V_{DFT} = The PV calculated by CO_2 physisorption using the DFT theory. N_2 S_{BET} = The SSA calculated by N_2 physisorption using the BET theory. CO_2 S_{DFT} = The SSA calculated by CO_2 physisorption using the DFT theory. The total PV determined by gas physisorption V_g = N_2 V_{BJH} + CO_2 V_{DFT}. The total SSA determined by gas physisorption S_g = N_2 S_{BET} + CO_2 S_{DFT}.

3.3. SANS

The SANS profiles of the six OM samples are depicted in Fig. 7a. Consistent with previous SANS experiments (Cui et al., 2024; Sun et al., 2019,2018), a “flat” background scattering is observed in the high q region ($q > 0.1$ Å^{-1}). This background primarily results from hydrogen atoms in the OM and clay-associated water (Wen et al., 2024; Bahadur et al., 2015), which will be discussed in detail later. After converting the raw data into $q^4I(q)$ vs. q^4 plots, the slope of the linear fit corresponds to the background value. The background-subtracted raw data were then fitted using the IRENA macro-plugin in Igor software to obtain the pore size distribution (2–98 nm) and structural parameters (Fig. 7b, Table 2). The PV distributions of the six samples differ notably. YC1 and LM2 both

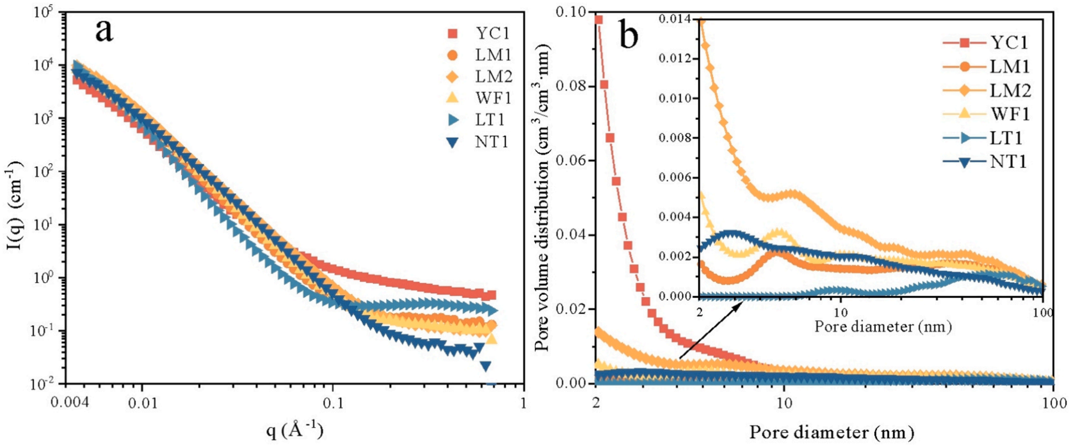

Fig. 7. (a) SANS profiles of OM samples. (b) PV distribution of OM samples obtained from SANS.

exhibit peaks at pore sizes smaller than 2 nm. LM1 and WF1 show multiple peaks, primarily at pore sizes below 2 nm and around 5 nm. NT1 has a single peak at approximately 3 nm, while LT1 displays a peak around 50 nm, the largest among all the samples. As shown in Fig. S1, YC1 has mass fractal characteristics, while the other five samples have surface fractal characteristics. Additionally, NT1 has the largest surface fractal dimension of 2.902, indicating that it has the greatest pore surface roughness.

It is noteworthy that the pore structure parameters obtained from SANS exhibit different trends compared to those derived from N_2 adsorption experiments (Fig. 8). Among the six samples, YC1 displays the highest SANS porosity (21.21 %), while NT1, which has the largest N_2 V_{BJH}, shows a porosity of only 9.91 %. Moreover, the porosity of NT1 is significantly lower than that of LM1, LM2, and WF1, despite these samples exhibiting lower N_2 V_{BJH} values. The difference between SANS and N_2 adsorption-derived results suggests that YC1, LM1, LM2, and WF1 have a higher fraction of closed pores than NT1, since SANS can characterize both connected and closed pores (Sun et al., 2020a,2024), whereas low-pressure N_2 adsorption only probes connected pores, these results highlight the differences in pore connectivity between the samples. Although LT1 exhibits a similar N_2 V_{BJH} to YC1, LM1, LM2, and WF1, its SANS porosity is only 7.11 %, indicating a lower proportion of closed pores.

3.4. WVA

3.4.1. WVA isothermal curves

The adsorption/desorption isotherms of water vapor for the six OM samples at 298.15 K, within the RH range of 0.002 to 0.95, are shown in Fig. 9. At low RH range (RH < ~0.2), the WVA capacity increases rapidly, indicating that monolayer adsorption dominates as moisture adsorbs onto primary sites. In the moderate RH range (approximately 0.2 < RH < 0.7), the isotherm shows a nearly linear increase, suggesting that multilayer adsorption becomes more prevalent, with adsorption on secondary sites gradually increasing. In the high RH range (RH > ~0.7), the WVA capacity increases steeply, signifying that capillary condensation is the dominant process (Xie et al., 2023; Yang et al., 2020). All samples meet the Type-H3 hysteresis loop and Type II isotherm based on the shape of the isothermal adsorption/desorption curves (Sing, 1985). Among the samples, LT1 exhibits the greatest difference between adsorption and desorption curves, while WF1 exhibited the smallest difference. This is primarily attributed to variations in pore surface properties and pore structures across the samples. Therefore, the degree of hysteresis observed in the curves reflects significant differences in the surface characteristics and pore structures of the six samples. Additionally, significant differences in WVA capacity were observed among the six samples when RH = 0.95 ($Q_{0.95}$). NT1 and LT1 both had $Q_{0.95}$ values exceeding 300 mg/g, much higher than the other four samples (19.29 to 41.14 mg/g) (Fig. 9 and Table 4).

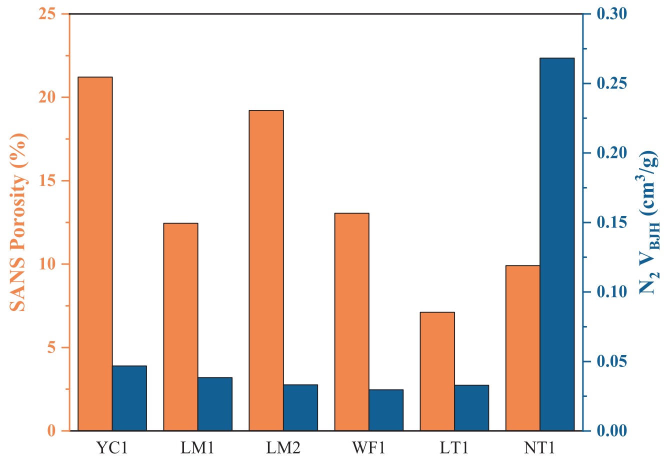

Fig. 8. SANS Porosity and N_2 V_{BJH} of OM samples.

3.4.2. Dent model analysis

The Dent model fits all of the WVA results well, with R^2 values all greater than 0.99 (Fig. 10, Table 4). As illustrated in Fig. 10, during the low RH stage (RH < ~0.2), all OM samples, except for NT1, exhibit a rapid increase in primary adsorption. In this stage, primary adsorption significantly exceeds secondary adsorption, indicating that water molecules are quickly adsorbed onto pore surfaces with strong binding forces. As RH continues to rise (~0.2 < RH < ~0.7), primary adsorption gradually reaches equilibrium, while secondary adsorption becomes more prominent, signaling the onset of multilayer adsorption. At the high RH stage (RH > ~0.7), secondary adsorption increases sharply, suggesting that capillary condensation becomes the dominant process. These observations are consistent with previous studies (Xie et al., 2023; Wang et al., 2019). For all samples, at RH 0.95, secondary adsorption greatly exceeds primary adsorption, highlighting that multilayer adsorption and capillary condensation dominating the water adsorption of OM. Notably, during RH < 0.2, the primary adsorption of NT1 does not exhibit a rapid increase but instead follows a nearly linear increasing pattern (Fig. 10). This could be attributed to the weaker binding forces between its primary sites and water molecules.

As shown in Table 4, the order of q_m for the six OM samples is LM2 < WF1 < YC1 < LM1 < LT1 < NT1. NT1 exhibits the highest q_m, which may be due to its significantly higher SSA (S_g) compared to the other samples (Table 3), providing more primary adsorption sites. In contrast, LT1, although it has a S_g 2–4 times larger than the other four samples

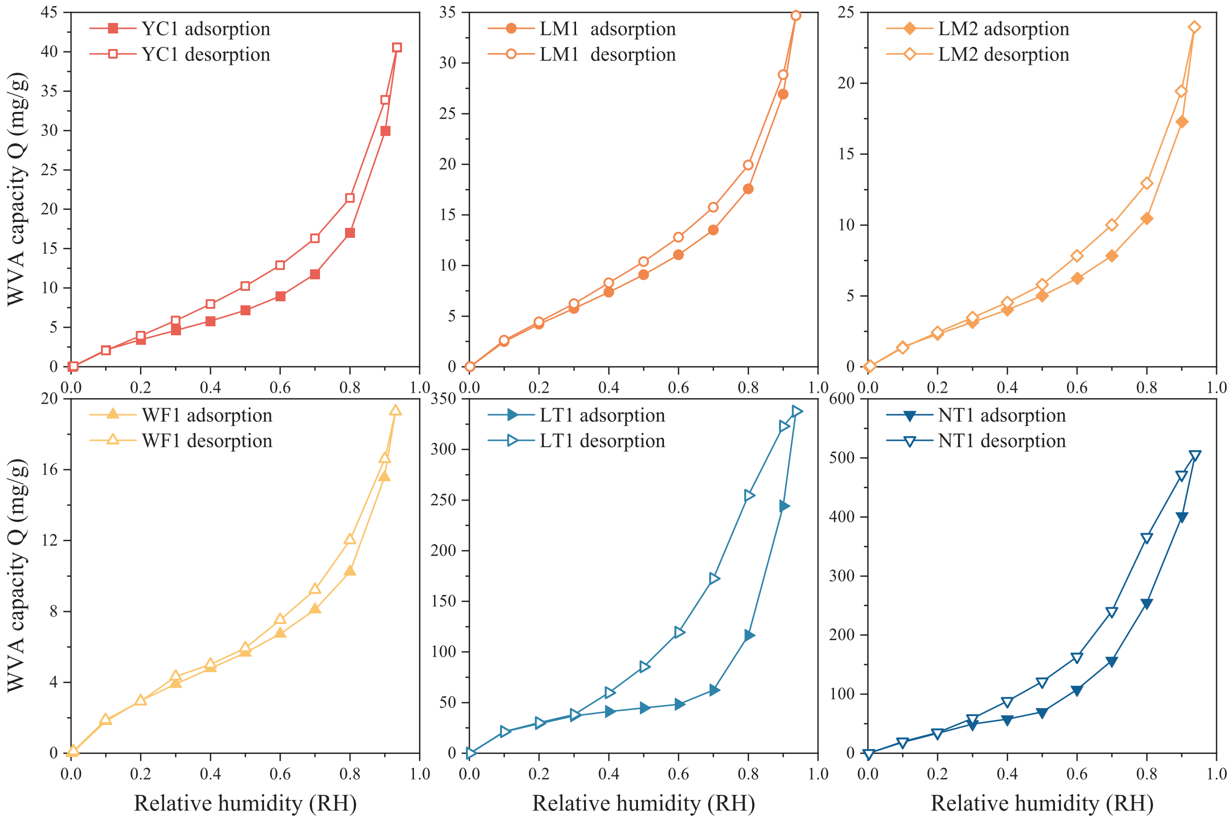

Fig. 9. WVA isotherms obtained from OM samples.

Table 4
Parameters of water vapor adsorption and model fitting results.

Sample ID	$Q_{0.95}$ (mg/g)	Dent model				Freundlich model						
		q_m (mg/g)	K_1	K_2	R^2	High strength regime			RH_c	Low strength regime		
						k(mg/g)	n	R^2		k(mg/g)	n	R^2
YC1	41.04	4.00	9.949	0.965	0.999	12.374	1.283	0.990	0.6682	48.643	0.240	0.966
LM1	35.13	5.13	10.046	0.909	0.997	16.910	1.171	0.992	0.7492	43.790	0.241	0.983
LM2	24.13	2.65	12.373	0.949	0.997	9.491	1.160	0.985	0.7494	31.409	0.200	0.974
WF1	19.29	3.10	16.007	0.899	0.996	9.877	1.333	0.994	0.7541	24.918	0.248	0.986
LT1	342.68	24.49	26.830	0.991	0.993	62.296	2.149	0.996	0.6852	460.080	0.174	0.990
NT1	512.40	90.55	1.071	0.900	0.997	126.204	1.214	0.996	0.5589	582.833	0.290	0.987

Note: $Q_{0.95}$ = Maximal WVA capacity at RH 0.95. q_m = The maximum WVA capacity via monolayer adsorption, mg/g. K_1 = Adsorption constants that reflect the adsorption strength between primary sites and water molecules. K_2 = Adsorption constants that reflect the adsorption strength between secondary sites and water molecules. n = a constant that describes the adsorption strength; k = a constant for WVA capacity, mg/g. RH_c = The critical relative humidity between high-intensity adsorption and low-intensity adsorption regions.

(Table 3), has a q_m value 5–9 times higher than these samples. This might be because its surface contains oxygen-containing functional groups that are highly hydrophilic (Ukaomah et al., 2023; Sang et al., 2019). Moreover, LT1 has the highest K_1 and K_2, indicating that the binding strength between its primary and secondary sites and water molecules is stronger than that of the other samples. In contrast, the lack of hydrophilic functional groups in NT1 likely explains its extremely low K_1 and K_2 values.

3.4.3. Freundlich model analysis

Plotting the WVA data of OM in the form of lnQ vs lnRH (Fig. 11), each sample can be divided into two distinct linear regions. The intersection point of the two lines corresponds to the critical relative humidity RH_c (Fig. 11, Table 4), which represents the transition between the two adsorption regions. Based on the values of n (Table 4), the two regions can be classified as high-intensity adsorption and low-intensity adsorption regions, located at relatively lower and higher RH ranges, respectively. At higher RH stages, water molecules form capillary condensation through weak dipole–dipole interactions, resulting in extremely low adsorption strength in this region (Yang et al., 2021; Sang et al., 2019; Feng et al., 2018). Therefore, regions with low-intensity represent adsorption dominated by capillary condensation, while regions with high-intensity represent layered adsorption.

The monolayer and multilayer WVA capacities of water are represented by the values of k in the high-intensity adsorption region, with the following order: LM2 < WF1 < YC1 < LM1 < LT1 < NT1 (Table 4). This sequence aligns with the q_m values from the Dent model, suggesting a correlation between the two parameters and implying that monolayer adsorption may serve as the foundation for multilayer adsorption. In the low-intensity adsorption region, the k values correspond to the WVA capacity associated with capillary condensation, following the order: WF1 < LM2 < LM1 < YC1 < LT1 < NT1 (Table 4). This pattern is

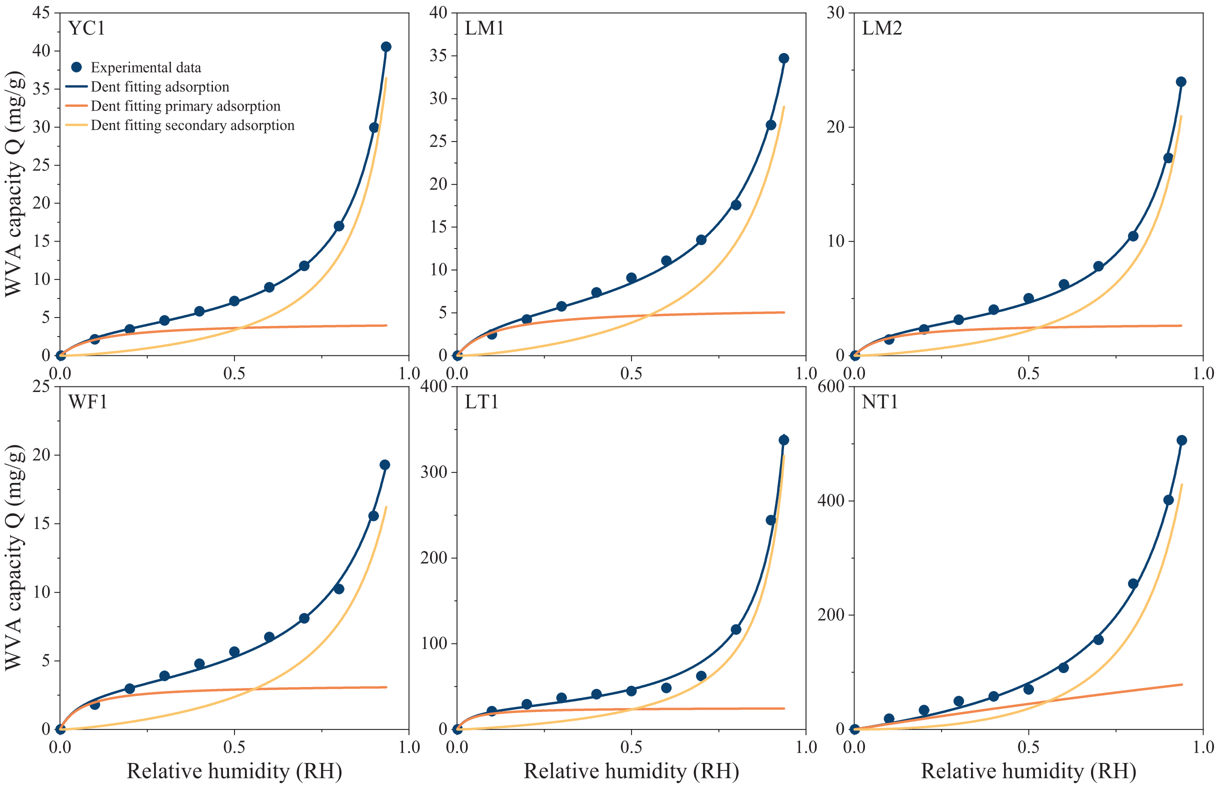

Fig. 10. WVA results of OM samples fitted with Dent model.

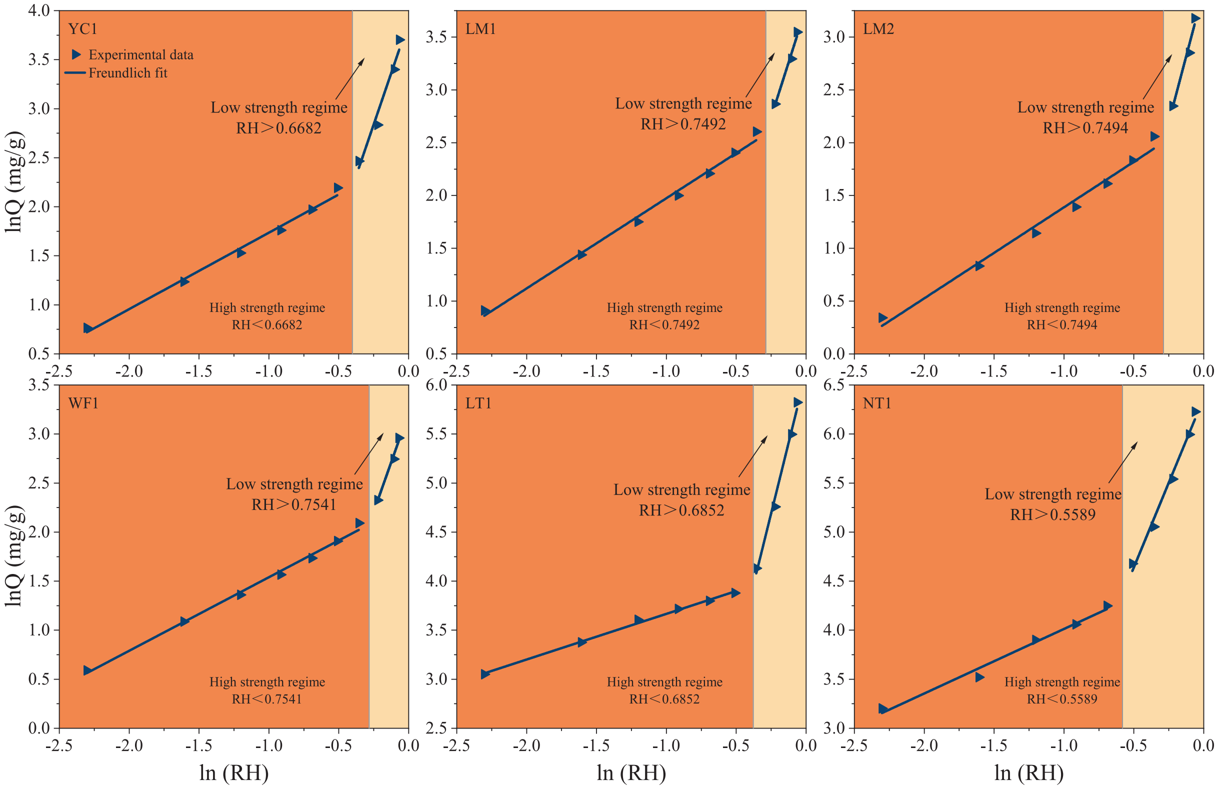

Fig. 11. WVA results of OM samples fitted with Freundlich model.

consistent with the experimentally determined WVA capacity at RH 0.95, where capillary condensation becomes dominant. Notably, LT1 exhibits a significantly higher n value (2.149) in the high-intensity adsorption region compared to the other samples, while the n values for the remaining samples are approximately 1.2. This suggests that water molecules adsorbed on the pore surfaces of LT1 are more intense than that in the other samples, which is agrees with the Dent model results. In the low-intensity adsorption region, the n values for all samples are less than 1, typically around 0.2. This region is characterized by capillary condensation, where the interactions between the pore walls and condensed water molecules are weak, primarily governed by intermolecular forces between water molecules. As a result, the n values are smaller and show little variation across the samples.

Combining the fitting results of the Dent and Freundlich models, the monolayer WVA capacity (Q_{mo}), multilayer WVA capacity (Q_{mu}), and capillary condensation WVA capacity (Q_{cc}) for each sample at RH 0.95 were calculated (Table 5). The Q_{mo} is calculated using Eq. (3) when RH = 0.95. The Q_{mu} is calculated using Eq. (4) when RH = RH_c. The Q_{cc} is calculated using Eq. (4) when $RH_c < RH < 0.95$.

4. Discussion

4.1. Controlling factors for WVA of OMs

4.1.1. Pore surface properties

Oxygen-containing functional groups in OM are generally considered hydrophilic and are believed to enhance WVA (Li et al., 2023b; Bai et al., 2020; Sang et al., 2019). In contrast, aliphatic structures are typically viewed as hydrophobic and incapable of adsorbing water molecules (Zhang et al., 2022; Zolfaghari et al., 2017b; Zeng et al., 2015). However, findings from this study reveal that although LM2 contains hydroxyl groups (–OH) and YC1 is dominated by aliphatic groups ($–CH_2$ and $–CH_3$), YC1 exhibits a higher monolayer WVA capacity (q_m = 4.00 mg/g) compared to LM2 (q_m = 2.65 mg/g) (Fig. 4, Table 4). This Indicates that OM surfaces dominated by aliphatic structures can also participate in water adsorption. Nevertheless, the lower adsorption strength constant (K_1) of YC1 indicates weaker interaction between its surface and water molecules relative to LM2 (Table 4). This observation is consistent with the simulation results of Li et al. (2023a), which showed that the relative coordination number of water molecules for $–CH_2$ groups was comparable to that for oxygen-containing functional groups such as C=O, C–O–C, and –OH. Moreover, since OM hydrophilicity is largely determined by the abundance of functional groups (Hu et al., 2016), the higher q_m observed in YC1 may also reflect the relatively lower hydroxyl content in LM2.

Previous experimental and simulation studies have demonstrated that carboxyl groups (–COOH) exhibit substantially stronger hydrophilicity than other common functional groups such as –OH, C=O, $–CH_2$, and $–CH_3$ (Li et al., 2023a; Zhang et al., 2015). Consistent with these findings, the results of this study show that LT1, which is enriched in –COOH, exhibits significantly higher monolayer WVA capacity (q_m) and surface adsorption strength (K_1) compared to LM1, LM2, and WF1, which predominantly contain –OH groups (Table 4). This indicates that –COOH contributes more effectively to enhancing OM surface hydrophilicity. Moreover, the markedly higher K_2 value of LT1 relative to other samples suggests that this stronger hydrophilicity can even affect the secondary adsorption above the monolayer, resulting in stronger binding of secondary sites with water molecules than in other samples.

It is noteworthy that NT1 exhibits a significantly higher q_m (90.55 mg/g) than all other samples, despite lacking hydrophilic functional groups. According to SANS-derived fractal dimension results, NT1 possesses the highest pore surface roughness (Fig. S1), which is known to generate a large number of adsorption sites (Chiang et al., 2020). While such rough surfaces promote increased WVA capacity, they are also associated with slower adsorption (Gordillo and Martí, 2010; A Manaf et al., 2019). As a result, NT1 does not exhibit the rapid adsorption observed in other samples at low RH stage (Fig. 10). Moreover, the absence of hydrophilic functional groups in NT1 results in weak surface interaction with water molecules, as indicated by its low K_1 value (1.071, Table 4). This weak interaction likely impairs multilayer adsorption. As shown in Fig. 12, the Q_{mu} of NT1 is significantly lower than its Q_{mo}, whereas in other samples, Q_{mu} is approximately twice that of Q_{mo}. As the number of adsorption layers increases, the water molecules become more distanced from the surface, reducing the interaction between pore surface and water molecules (Yang et al., 2021), thereby limiting multilayer adsorption. Nevertheless, at high RH stage, the water molecules already adsorbed within the pores act as anchor sites for capillary condensation (Zhang et al., 2022). Therefore, while NT1′s weak surface–water interactions constrain multilayer adsorption, they do not inhibit capillary condensation at high RH.

Table 5
Monolayer adsorption, multilayer adsorption, and capillary condensation of water vapor adsorption.

Sample ID	Q_{mo} (mg/g)	Q_{mu} (mg/g)	Q_{cc} (mg/g)
YC1	3.96	6.72	29.72
LM1	5.05	10.37	18.69
LM2	2.62	6.24	14.71
WF1	3.07	6.32	9.90
LT1	24.42	50.58	268.64
NT1	78.48	21.14	407.64

Note: Q_{mo} = the monolayer WVA capacity at RH 0.95. Q_{mu} = multilayer WVA capacity at RH 0.95. Q_{cc} = capillary condensation WVA capacity at RH 0.95.

4.1.2. Pore structure

PV and SSA are commonly regarded as key factors influencing WVA capacity (Sang et al., 2018; Bai et al., 2020). However, due to the polarity of water molecules, significant differences exist between WVA and the physisorption behavior of non-polar gases (Thommes et al., 2013). Although a general positive correlation is observed between the OM SSA (S_g) and q_m, as well as between the PV (V_g) and $Q_{0.95}$, notable deviations are present—for instance, in the cases of LT1 and NT1 (Fig. 13a,b). To further explore these inconsistencies, BET theory was applied using a water molecule cross-sectional area of 0.0106 nm^2 (Newman, 1983) to calculate the WVA–derived SSA (S_w). In addition, $Q_{0.95}$ was converted to the corresponding water volume by assuming a density of 1 g/cm^3, representing the effective pore volume filled by water (V_w). By comparing the pore structure parameters derived from WVA with those obtained from gas physisorption (N_2 and CO_2), a more intuitive and comprehensive understanding of the discrepancies between these two measurement approaches can be achieved.

As shown in Fig. 14a, the V_w of LT1 and NT1 is 7.65 and 1.88 times greater than their V_g, respectively. In contrast, for the other samples, V_w

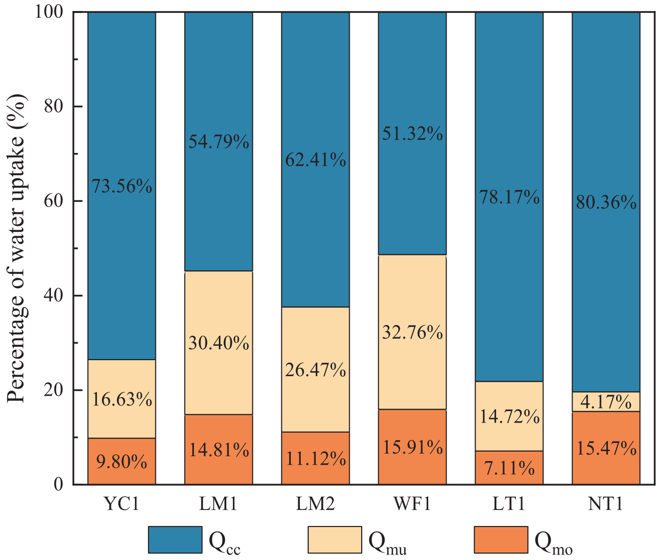

Fig. 12. Percentage of WVA at RH 0.95 ($Q_{0.95}$) based on the classification of monolayer absorption (Q_{mo}), multilayer adsorption (Q_{mu}), and capillary condensation (Q_{cc}).

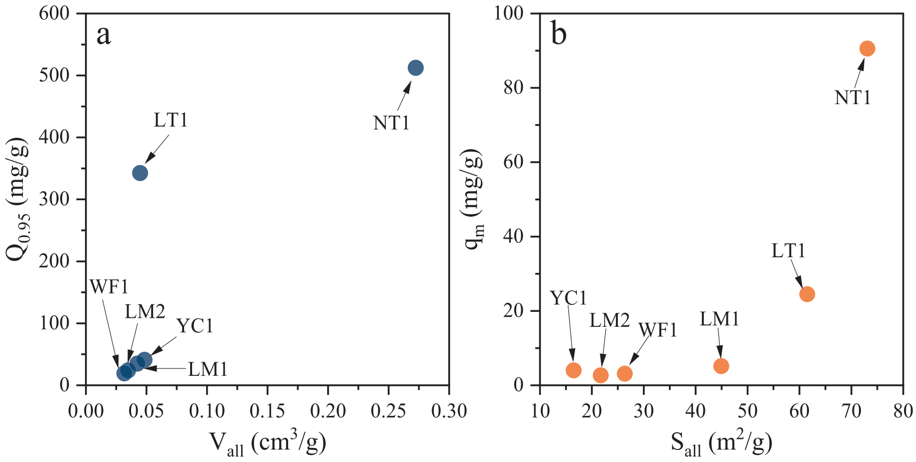

Fig. 13. (a) Relationship between V_g and $Q_{0.95}$; The total PV determined by gas physisorption $V_g = N_2\ V_{BJH} + CO_2\ V_{DFT}$; $Q_{0.95}$ = Maximal WVA capacity at RH 0.95. (b) Relationship between S_g and q_m; The total SSA determined by gas physisorption $S_g = N_2\ S_{BET} + CO_2\ S_{DFT}$; q_m = The maximum amount of monolayer adsorption, mg/g.

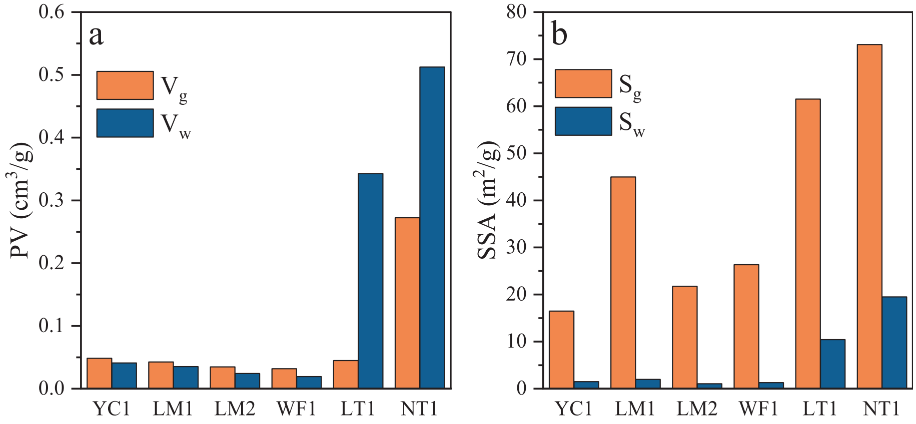

Fig. 14. (a) V_g and V_w of OM samples; V_w = the PV filled by water. (b) S_g and S_w of OM samples; S_w = the SSA for WVA.

is smaller than V_g. This indicates that, in LT1 and NT1, the pore size range participating in WVA extends beyond the gas physisorption techniques, which typically characterize pores smaller than ~200 nm. It also implies that the pores involved in WVA in LT1 and NT1 are larger in diameter than those in the other samples. A previous study demonstrated that, under a given RH, stronger hydrophilicity (a smaller contact angle between the adsorbent and water) promotes water condensation in larger pores (Zolfaghari et al., 2017b). Therefore, the involvement of larger pores in LT1 may be attributed to the presence of strongly hydrophilic –COOH groups. In contrast, NT1 exhibits extremely low hydrophilicity, suggesting that other factors must account for its broad WVA-active pore size range. Compared to the other samples, NT1 displays lower closed porosity (see Section 3.3), a more uniform pore size distribution, and a lower proportion of micropores (Fig. 15), all of which contribute to improved pore connectivity. Previous studies have shown that water already adsorbed in shale can block pore throats and hinder subsequent water vapor diffusion and adsorption (Meng et al., 2024; Feng et al., 2018). Liu et al. (2022) further noted that poor pore connectivity exacerbates this blocking effect. Therefore, the superior connectivity of NT1, although not directly investigated, likely facilitates water transport within the pore network, mitigates blockage formation, and enables WVA to occur across a wider range of pore sizes (Mason, 1982).

As shown in Fig. 14b, the S_w is significantly lower than the S_g for all samples, indicating that the water adsorption sites are localized rather than covering the entire pore surface. This contrasts with findings from previous studies on shale and clay minerals, where S_w often exceeds S_g. Such discrepancies may be attributed to the expansive nature and strong hydrophilicity of clay minerals, as well as the inability of nitrogen to access pores smaller than 2 nm, which can lead to an underestimation of SSA by gas physisorption and an overestimation by WVA (Xiong et al., 2023; Sang et al., 2019). Notably, LT1 and NT1 exhibit S_w/S_g ratios of 16.96 % and 26.66 %, respectively, which are significantly higher than those of the other four samples (ranging from 4.41 % to 9.06 %) (Fig. 14b). This is partially due to the broader pore size range involved in WVA for LT1 and NT1, as discussed earlier. Moreover, it suggests that the density of water adsorption sites on their pore surfaces is higher than in the other samples. This can be primarily attributed to two factors: (1) the type and abundance of surface functional groups and their corresponding water coordination numbers (Li et al., 2023a), and (2) the great number of adsorption sites associated with rough surface (Chiang et al., 2020; Gordillo and Martí, 2010).

As shown in Fig. 12, the proportion of Q_{cc} to $Q_{0.95}$ for all samples exceeds 50 %, with a maximum of 80.36 %, indicating that capillary condensation occupies a dominant fraction in the WVA of OM. This finding aligns with previous studies (Xing et al., 2025; Zhang et al., 2022). This is primarily attributed to the mesopore PV of these OM samples, which accounts for more than 50 % of the total PV (Fig. 15), providing ample space for capillary condensation of water vapor (Sang et al., 2019).

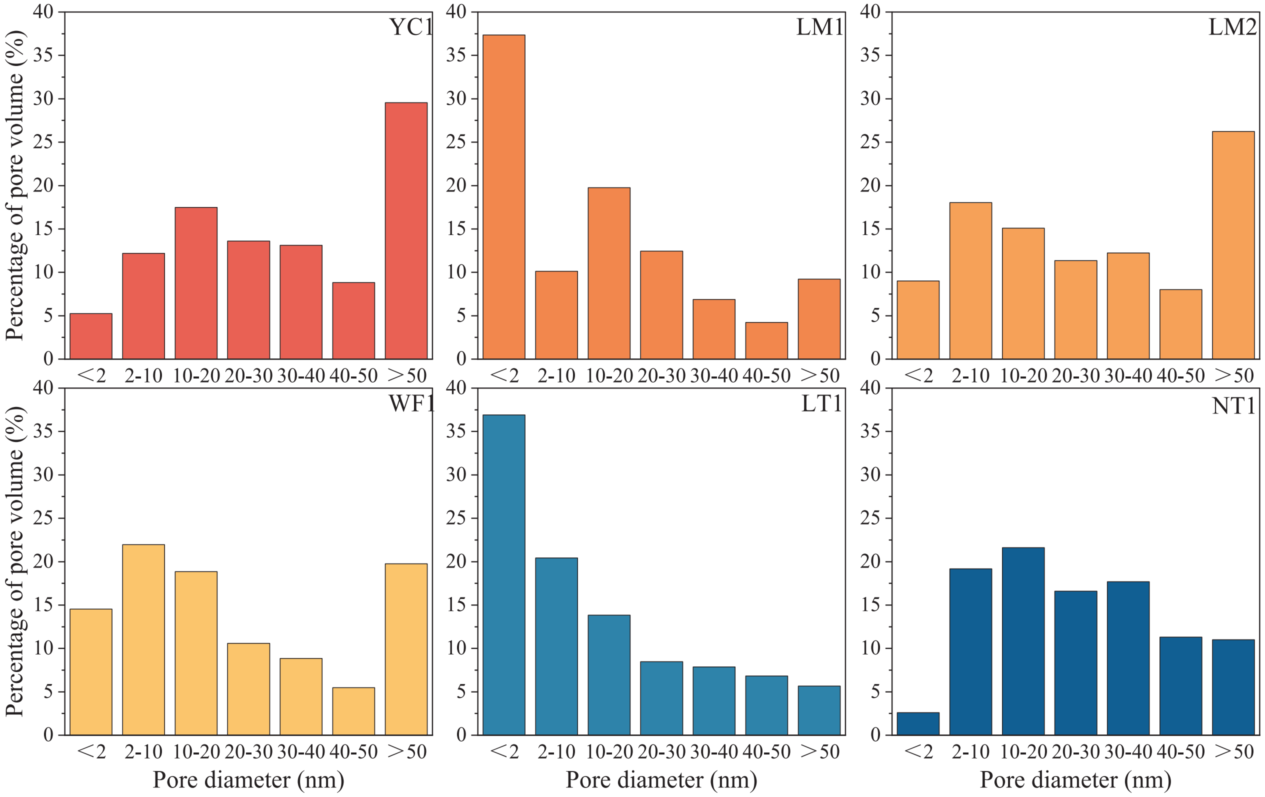

Fig. 15. Percentage of PV for OM samples obtained by gas physisorption.

4.2. OMs vs. WVA

OM with different types, maturities, and thermal evolution histories inevitably exhibits varying WVA behaviors, due to differences in pore surface properties and pore structures.

4.2.1. OM types vs. pore structures and surface properties

During thermal evolution, OM forms secondary organic pores in conjunction with hydrocarbon generation. Owing to compositional differences, different OM types exhibit distinct hydrocarbon generation behaviors and associated pore characteristics (Liu et al., 2022). Type I and Type II OM, which are rich in liptinite, have strong hydrocarbon generation potential and typically develop well-defined pore structures. In contrast, Type III OM, predominantly composed of vitrinite, has much lower hydrocarbon generation capacity (Liu et al., 2022). For instance, Hui et al. (2024) reported that the initial hydrocarbon generation potential of Type I kerogen can reach 790 mg/g, whereas that of Type III kerogen is only 85 mg/g. Similarly, Chen et al. (2015) demonstrated that the organic pore development potential declines progressively from Type I to Type III OM, with Type I exhibiting pore development capabilities up to tens of times greater than those of Type III. As shown in Table 3, Type I OM (YC1 and NT1) possesses higher PV than both Type II (LM1, LM2, WF1) and Type III (LT1) OM. Previous studies have indicated that Types I and II primarily develop mesopores (2–50 nm) and macropores (>50 nm), while Type III OM is dominated by micropores (<2 nm) (Chalmers and Bustin, 2008). These observations are consistent with the FE-SEM imaging results (Fig. S2). Furthermore, CO_2 adsorption data confirm that Type III OM (LT1) has a very high SSA, attributable to its high micropore content (Table 3). Among the three OM types, Type I (YC1 and NT1) exhibits the largest PVs (0.0484–0.2724 cm^3/g) and the lowest micropore fractions (2.61–5.25 %). In contrast, Types II and III display smaller PVs (0.0317–0.0448 cm^3/g) and significantly higher micropore fractions (9.00–37.35 %) (Table 3, Fig. 15). These results suggest that Types II and III have lower pore connectivity than Type I OM.

According to Tissot and Welte (1984), immature Type I OM ($H/C > 1.5$, $O/C < 0.1$) is primarily composed of long-chain aliphatic hydrocarbons. Type II OM ($1.0 < H/C < 1.5$, $0.1 < O/C < 0.2$) contains a greater proportion of cyclic aliphatic hydrocarbons and significant amounts of aromatic compounds. In contrast, Type III OM ($H/C < 1.0$, $0.2 < O/C < 0.3$) is dominated by aromatic structures and oxygen-containing functional groups. These compositional differences lead to distinct functional group distributions among OM types. As shown in Fig. 4, Type I OM (YC1) is consists primarily of aliphatic structures and lacks oxygen-containing functional groups. In contrast, Type II OM samples (LM1, LM2, and WF1) mainly contains hydroxyl groups, while Type III OM (LT1) is primarily enriched in carboxyl groups (Salmon et al., 2011; Robin and Rouxhet, 1978).

4.2.2. Maturity vs. pore structures and surface properties

Immature or low-maturity OM has not undergone significant thermal cracking or hydrocarbon expulsion and thus retains its original low-porosity structure. According to Loucks et al. (2012), the development of secondary organic pores begins at a minimum maturity level of approximately R_o 0.6 %. As maturity increases, these secondary pores progressively evolve (Cao et al., 2015). In overmature OM, extensive hydrocarbon generation and expulsion lead to the formation of abundant nanoscale pores, particularly upon entering the "gas window" (Curtis et al., 2012). Liu et al. (2022) found that PV and SSA increase with maturity, peaking at R_o 2.5–3.0 % before decreasing as maturity continues to increase, eventually approaching the poorly developed pore structure of graphite.

Although the SSA of OM appears to be positively correlated with maturity (Fig. 16a), this relationship may be coincidental. This is primarily because different OM types undergo distinct pore evolution pathways during thermal maturation, owing to their diverse chemical compositions (Borjigin et al., 2021). Recent studies have shown that the hydrocarbon generation window for Type I kerogen is narrower than

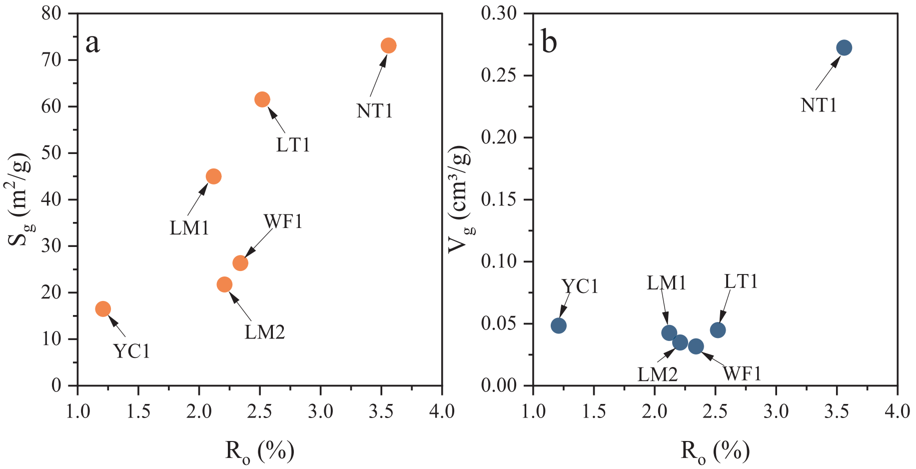

Fig. 16. (a) Relationship between R_o and S_g. (b) Relationship between R_o and V_g.

that for Types II and III (Wang et al., 2025), and the threshold R_o values for hydrocarbon generation increase progressively from 0.42 % to 0.74 % across Types I to III (Hui et al., 2024). As a result, the PV of the six OM samples investigated does not exhibit a consistent trend with increasing maturity (Fig. 16b). However, among Type II OM samples (LM1, LM2, and WF1), both SSA and PV tend to decrease as maturity increases from R_o 2.12 % to 2.34 % (Fig. 16). This observation aligns with previous findings reporting a decline in PV beyond a maturity threshold of R_o 2.0–2.47 % (Zhang et al., 2020). Moreover, the evolution of organic pores is not solely governed by OM type and maturity. Rigid minerals within the shale matrix play a crucial role in preserving pore structures by mitigating compaction-related damage (Knapp et al., 2020; Fishman et al., 2012). For instance, the high quartz content in NT1 (74 %) likely contributes to its relatively high PV and SSA despite its overmature state (R_o 3.56 %).

Liu et al. (2019) reported that with increasing maturity, Bakken shale exhibits a more uniform pore-throat size distribution and a more homogeneous pore structure. Similar trends are observed in Fig. 15. For Type I OM samples (YC1 and NT1), the more mature NT1 displays a lower proportion of micropores and a more uniform pore size distribution. Likewise, for Type II OM samples (LM1, WF1, and LM2), increasing maturity is associated with a reduced micropore fraction and improved uniformity in pore size distribution, which enhances pore connectivity. However, with continued thermal evolution beyond the overmature stage, OM graphitization may lead to pore collapse or closure, ultimately impairing pore connectivity (Xue et al., 2022).

With increasing maturity, the functional groups of OM in shale undergo systematic changes, including shortening of aliphatic chains, enhanced aromaticity, depletion of oxygen-containing groups, and increased graphitization (Liang et al., 2024; Hackley et al., 2017; Stock et al., 2017). Consistent trends are observed in this study. As shown in Fig. 17, the SANS flat background decreases with increasing maturity. Given that this background signal is associated with hydrogen content in OM (Bahadur et al., 2015), the decline indicates a progressive loss of hydrogen, reflecting the shortening of aliphatic chains (Liang et al., 2024). Moreover, as R_o increases, the aliphatic structure in Type I OM (YC1 and NT1) and hydroxyl groups in Type II OM (LM1, LM2, and WF1) weaken in the FTIR spectra (Fig. 4). The SANS-derived surface fractal dimension also increases with maturity (Fig. S1), indicating greater pore surface roughness (Tian et al., 2024; Chiang et al., 2020; Sun et al., 2020b). However, the LT1 (Type III OM) deviates markedly from these evolutionary trends in terms of SANS flat background (Fig. 17), functional group evolution (Fig. 4), and surface fractal dimension (Table 2). This deviation likely reflects a distinct thermal transformation pathway for Type III OM, differing fundamentally from those of Types I and II (Hui et al., 2024; Tissot and Welte, 1984).

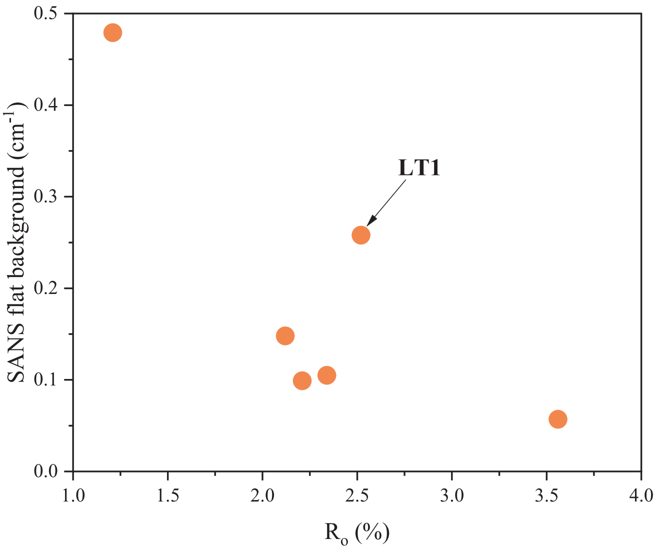

Fig. 17. Relationship between R_o and SANS flat background of OM samples.

4.2.3. WVA mode of OMs

The adsorption of water vapor by OM is governed by two primary factors: pore surface properties (including functional group type, functional group content, and surface roughness) and pore structure (SSA, PV, and pore connectivity). The observed WVA behavior thus results from the interplay between these structural and chemical characteristics. SSA and PV provide the physical basis for WVA (Yang et al., 2020; Sang et al., 2018). Specifically, the pore surface area enables monolayer adsorption, while pore volume accommodates multilayer adsorption and capillary condensation. Meanwhile, the pore surface chemistry controls both the number of adsorption sites and the strength of interaction between water molecules and the surface. Different functional groups exhibit varying water coordination number (Li et al., 2023a); hence, the type and abundance of functional groups determine the density of adsorption sites. Experimental results from this study (Table 4, K1 values) reveal that samples containing different functional groups display distinct water adsorption strengths, following the trend: $-COOH$ (LT1) > $-OH$ (LM1, LM2, WF1) > $-CH_2/-CH_3$ (YC1) > rough surfaces lacking functional groups (NT1). As the number of adsorption layers increases, the interaction between the pore surface and adsorbed water molecules diminishes (Yang et al., 2021), indicating that multilayer adsorption is also influenced by initial surface adsorption strength. Additionally, OM samples with stronger hydrophilicity (LT1) or better pore connectivity (NT1) exhibit broader pore size distributions for WVA compared to other samples (Zolfaghari et al., 2017b; Mason, 1982). In summary, both pore surface properties and pore structure co-regulate the WVA behavior of OM. The differences in these characteristics among OM of varying types and maturities ultimately account for the observed diversity in their adsorption performance.

For instance, YC1 (Type I), although the least mature sample, exhibits a higher PV than the more mature Type II samples LM1, LM2, and WF1, resulting in a correspondingly higher $Q_{0.95}$. While its aliphatic structures confer relatively weak adsorption strength toward water molecules, YC1 possesses more adsorption sites than WF1 and LM2, leading to a higher monolayer WVA capacity (q_m). LT1 (Type III) has a PV comparable to that of YC1; however, the presence of strongly hydrophilic carboxyl groups contributes to significantly greater $Q_{0.95}$, q_m, and surface adsorption strength. NT1 (Type I), with substantially higher maturity than YC1, demonstrates both larger PV and enhanced pore connectivity. Despite lacking functional groups, its rough pore surfaces offer numerous adsorption sites. As a result, NT1 exhibits exceptionally high $Q_{0.95}$ and q_m values, although the adsorption strength of its surface remains very low.

It should be noted that, due to the limited number of samples and the relatively narrow maturity range investigated, the findings presented here may be subject to biases. In future work, we will perform pyrolysis on three types of immature OM to generate a series of samples with progressively increasing maturity. This will enable a quantitative assessment of how the physicochemical characteristics and WVA capacity of different OM types evolve with maturity, thereby providing a more comprehensive understanding of OM–water interactions and WVA behavior.

5. Conclusion

This study is the first to systematically compare the WVA behavior of OM samples with varying types and maturities. FTIR and SANS techniques were innovatively integrated to characterize the surface properties of OM, including functional groups and surface roughness. Key factors governing the WVA behavior of OM were identified. Based on the experimental findings, the following conclusions are drawn:

1. WVA of OM increases progressively with RH. Initially, monolayer adsorption occurs sporadically on the pore surfaces, followed by multilayer adsorption that leads to capillary condensation. Notably, capillary condensation—primarily occurring in mesopores—plays a dominant role in the WVA behavior of OM.
2. The WVA behavior of OM results from the coupled effects of pore surface properties and pore structure. SSA and PV provide the spatial foundation for adsorption, while pore surface properties—including functional group types, functional group abundance, and surface roughness—govern the adsorption strength, number of adsorption sites, and the extent of multilayer adsorption. Furthermore, the hydrophilicity and pore connectivity collectively determine the range of pore sizes involved in the adsorption process.
3. Among the three types of OM, Type I appears to exhibits the greatest potential for secondary pore development and pore connectivity, providing the largest spatial capacity for water adsorption, despite lacking strongly hydrophilic functional groups. In contrast, Type III OM, despite having the lowest potential for pore development and connectivity, contains strongly hydrophilic functional groups (especially carboxyl groups), which greatly enhance WVA. Type II OM displays intermediate adsorption behavior, falling between types I and III.
4. The pore surface properties and pore structures of OM are strongly influenced by thermal evolution, resulting in distinct characteristics. For example, overmature samples (NT1) have significantly larger PV and SSA than mature samples of the same type (YC1), resulting in a greater WVA capacity. However, the absence of functional groups reduces adsorption strength. Additionally, different types of OM undergo distinct thermal evolution pathways, resulting in significant differences in WVA behavior among OM of different types and maturities.

CRediT authorship contribution statement

Jiajun Fu: Writing – original draft, Methodology, Investigation. **Ke Xu:** Writing – review & editing, Resources, Conceptualization. **Yeping Ji:** Writing – review & editing, Investigation. **Xuezhe Wang:** Methodology, Investigation, Data curation. **Yiquan Ma:** Writing – review & editing, Resources, Project administration. **Mehdi Ostadhassan:** Writing – review & editing, Data curation, Conceptualization. **Zhejun Pan:** Resources, Project administration, Conceptualization. **Duo Wang:** Methodology, Investigation, Data curation. **Bo Liu:** Resources, Project administration, Conceptualization. **Yubing Ke:** Methodology. **Mengdi Sun:** Writing – review & editing, Supervision, Conceptualization.

Declaration of competing interest

The authors declare that they have no known competing financial interests or personal relationships that could have appeared to influence the work reported in this paper.

Acknowledgements

The authors sincerely thank the National Natural Science Foundation (Grant Nos. 42272159 and U23A20596), and the Superior Youth Foundation of Heilongjiang Province (No. YQ2023D002) of China, for their financial support.

Appendix A. Supplementary data

Supplementary data to this article can be found online at https://doi.org/10.1016/j.jhydrol.2025.134223.

Data availability

The data that has been used is confidential.

References

A Manaf, N.D., Fukuda, K., Subhi, Z.A., Mohd Radzi, M.F., 2019. Influences of surface roughness on the water adsorption on austenitic stainless steel. Tribol. Int. 136, 75–81. https://doi.org/10.1016/j.triboint.2019.03.014.

Bahadur, J., Radlinski, A.P., Melnichenko, Y.B., Mastalerz, M., Schimmelmann, A., 2015. Small-Angle and Ultrasmall-Angle Neutron Scattering (SANS/USANS) study of new Albany shale: a treatise on microporosity. Energy Fuels 29, 567–576. https://doi.org/10.1021/ef502211w.

Bai, J., Kang, Y., Chen, M., Chen, Z., You, L., Li, X., Chen, G., 2020. Impact of surface chemistry and pore structure on water vapor adsorption behavior in gas shale. Chem. Eng. J. 402, 126238. https://doi.org/10.1016/j.cej.2020.126238.

Borjigin, T., Lu, L., Yu, L., Zhang, W., Pan, A., Shen, B., Wang, Y., Yang, Y., Gao, Z., 2021. Formation, preservation and connectivity control of organic pores in shale. Pet. Explor. Dev. 48, 798–812. https://doi.org/10.1016/S1876-3804(21)60067-8.

Brunauer, S., Emmett, P.H., Teller, E., 1938. Adsorption of gases in multimolecular layers. J. Am. Chem. Soc. 60, 309–319. https://doi.org/10.1021/ja01269a023.

Cao, T., Song, Z., Wang, S., Xia, J., 2015. A comparative study of the specific surface area and pore structure of different shales and their kerogens. Sci. China Earth Sci. 58, 510–522. https://doi.org/10.1007/s11430-014-5021-2.

Cardott, B.J., Curtis, M.E., 2018. Identification and nanoporosity of macerals in coal by scanning electron microscopy. Int. J. Coal Geol. 190, 205–217. https://doi.org/10.1016/j.coal.2017.07.003.

Chalmers, G.R.L., Bustin, R.M., 2008. Lower cretaceous gas shales in northeastern British Columbia, Part I: geological controls on methane sorption capacity. Bull. Can. Pet. Geol. 56, 1–21. https://doi.org/10.2113/gscpgbull.56.1.1.

Charrière, D., Behra, P., 2010. Water sorption on coals. J. Colloid Interf. Sci. 344, 460–467. https://doi.org/10.1016/j.jcis.2009.11.064.

Chen, Y., Qin, Y., Wei, C., Huang, L., Shi, Q., Wu, C., Zhang, X., 2018. Porosity changes in progressively pulverized anthracite subsamples: implications for the study of closed pore distribution in coals. Fuel 225, 612–622. https://doi.org/10.1016/j.fuel.2018.03.164.

Chen, Z., Wang, T., Liu, Q., Zhang, S., Zhang, L., 2015. Quantitative evaluation of potential organic-matter porosity and hydrocarbon generation and expulsion from mudstone in continental lake basins: a case study of Dongying sag, eastern China. Mar. Petrol. Geol. 66, 906–924. https://doi.org/10.1016/j.marpetgeo.2015.07.027.

Chiang, W.-S., Chen, J.-H., Jacobi, D., Yildirim, T., Turkoglu, D., Althaus, S., Liu, Y., 2020. Structural properties of kerogens with different maturities. Energy Fuels 34, 12354–12365. https://doi.org/10.1021/acs.energyfuels.0c02268.

Cui, Z., Sun, M., Mohammadian, E., Hu, Q., Liu, B., Ostadhassan, M., Yang, W., Ke, Y., Mu, J., Ren, Z., Pan, Z., 2024. Characterizing microstructural evolutions in low-mature lacustrine shale: a comparative experimental study of conventional heat, microwave, and water-saturated microwave stimulations. Energy 294, 130797. https://doi.org/10.1016/j.energy.2024.130797.

Curtis, J.B., 2002. Fractured shale-gas systems. AAPG Bull. 86. https://doi.org/10.1306/61EEDDBE-173E-11D7-8645000102C1865D.

Curtis, M.E., Cardott, B.J., Sondergeld, C.H., Rai, C.S., 2012. Development of organic porosity in the Woodford Shale with increasing thermal maturity. Int. J. Coal Geol. 103, 26–31. https://doi.org/10.1016/j.coal.2012.08.004.

Dang, W., Jiang, S., Zhang, J., Li, P., Nie, H., Liu, Y., Li, F., Sun, J., Tao, J., Shan, C., Tang, X., Wang, R., Yin, Y., 2021. A systematic experimental and modeling study of water adsorption/desorption behavior in organic-rich shale with different particle sizes. Chem. Eng. J. 426, 130596. https://doi.org/10.1016/j.cej.2021.130596.

Dent, R.W., 1977. A multilayer theory for gas sorption: Part II: Sorption of gas mixtures. Text. Res. J. 47, 188–198. https://doi.org/10.1177/004051757704700307.

Feng, D., Li, X., Wang, X., Li, J., Sun, F., Sun, Z., Zhang, T., Li, P., Chen, Y., Zhang, X., 2018. Water adsorption and its impact on the pore structure characteristics of shale clay. Appl. Clay Sci. 155, 126–138. https://doi.org/10.1016/j.clay.2018.01.017.

Feng, Y., Xiao, X., Gao, P., Hu, D., Liu, R., Li, G., Lu, C., Zhou, Q., 2024. Water distribution in pore systems and its influences on gas-bearing property of deep shale: a case study of the Longmaxi Formation in the Luzhou area, southern Sichuan Basin. Mar. Petrol. Geol. 163, 106805. https://doi.org/10.1016/j.marpetgeo.2024.106805.

Fishman, N.S., Hackley, P.C., Lowers, H.A., Hill, R.J., Egenhoff, S.O., Eberl, D.D., Blum, A.E., 2012. The nature of porosity in organic-rich mudstones of the Upper Jurassic Kimmeridge Clay Formation, North Sea, offshore United Kingdom. Int. J. Coal Geol. 103, 32–50. https://doi.org/10.1016/j.coal.2012.07.012.

Gasparik, M., Bertier, P., Gensterblum, Y., Ghanizadeh, A., Krooss, B.M., Littke, R., 2014. Geological controls on the methane storage capacity in organic-rich shales. Int. J. Coal Geol. 123, 34–51. https://doi.org/10.1016/j.coal.2013.06.010.

Gordillo, M.C., Martí, J., 2010. Effect of surface roughness on the static and dynamic properties of water adsorbed on graphene. J. Phys. Chem. B 114, 4583–4589. https://doi.org/10.1021/jp9114332.

Hackley, P.C., Walters, C.C., Kelemen, S.R., Mastalerz, M., Lowers, H.A., 2017. Organic petrology and micro-spectroscopy of Tasmanites microfossils: applications to kerogen transformations in the early oil window. Org. Geochem. 114, 23–44. https://doi.org/10.1016/j.orggeochem.2017.09.002.

Hu, Y., Devegowda, D., Sigal, R., 2016. A microscopic characterization of wettability in shale kerogen with varying maturity levels. J. Nat. Gas Sci. Eng. 33, 1078–1086. https://doi.org/10.1016/j.jngse.2016.06.014.

Hui, S., Pang, X., Jiang, F., Wang, C., Mei, S., Hu, T., Pang, H., Li, M., Zhou, X., Shi, K., 2024. Quantitative effect of kerogen type on the hydrocarbon generation potential of Paleogene lacustrine source rocks, Liaohe Western Depression, China. Pet. Sci. 21, 14–30. https://doi.org/10.1016/j.petsci.2023.09.004.

Katz, B.J., Arango, I., 2018. Organic porosity: a geochemist's view of the current state of understanding. Org Geochem. 123, 1–16. https://doi.org/10.1016/j.orggeochem.2018.05.015.

Knapp, L.J., Ardakani, O.H., Uchida, S., Nanjo, T., Otomo, C., Hattori, T., 2020. The influence of rigid matrix minerals on organic porosity and pore size in shale reservoirs: upper Devonian Duvernay Formation, Alberta. Canada. Int. J. Coal Geol. 227, 103525. https://doi.org/10.1016/j.coal.2020.103525.

Li, J., Li, B., Gao, Z., 2021. Water vapor adsorption behavior in shale under different temperatures and pore structures. Nat. Resour. Res. 30, 2789–2805. https://doi.org/10.1007/s11053-021-09846-0.

Li, W., Stevens, L.A., Zhang, B., Zheng, D., Snape, C.E., 2023a. Combining molecular simulation and experiment to understand the effect of moisture on methane adsorption in kerogens. Chem. Eng. J. 454, 139942. https://doi.org/10.1016/j.cej.2022.139942.

Li, Y., Zhai, C., Sun, Y., Xu, J., Yu, X., Huang, T., 2023b. Characterizing water vapor adsorption on coal by nuclear magnetic resonance: Influence of coal pore structure and surface properties. Energy 282, 128420. https://doi.org/10.1016/j.energy.2023.128420.

Liang, Z., Jiang, Z., Xue, Z., Qiao, P., Wu, W., Jiang, Y., Tang, X., Chen, R., Arif, M., 2024. Molecular structure and evolution mechanism of shale kerogen: insights from thermal simulation and spectroscopic analysis. J. Anal. Appl. Pyrol. 181, 106648. https://doi.org/10.1016/j.jaap.2024.106648.

Liu, B., Mastalerz, M., Schieber, J., 2022a. SEM petrography of dispersed organic matter in black shales: a review. Earth Sci. Rev. 224, 103874. https://doi.org/10.1016/j.earscirev.2021.103874.

Liu, B., Schieber, J., Mastalerz, M., 2017. Combined SEM and reflected light petrography of organic matter in the New Albany Shale (Devonian-Mississippian) in the Illinois Basin: a perspective on organic pore development with thermal maturation. Int. J. Coal Geol. 184, 57–72. https://doi.org/10.1016/j.coal.2017.11.002.

Liu, G., Xie, S., Tian, W., Wang, J., Li, S., Wang, Y., Yang, D., 2022b. Effect of pore-throat structure on gas-water seepage behaviour in a tight sandstone gas reservoir. Fuel 310, 121901. https://doi.org/10.1016/j.fuel.2021.121901.

Liu, K., Ostadhassan, M., Kong, L., 2019. Fractal and multifractal characteristics of pore throats in the Bakken shale. Transp. Porous Med. 126, 579–598. https://doi.org/10.1007/s11242-018-1130-2.

Liu, S., Ma, W., Luba, J., Huang, W., Zeng, X., Zhang, C., 2011. Characteristics of the shale gas reservoir rocks in the lower Silurian Longmaxi Formation, East Sichuan basin. China. Acta Petrol. Sin. 27, 2239–2252.

Loucks, R.G., Reed, R.M., Ruppel, S.C., Hammes, U., 2012. Spectrum of pore types and networks in mudrocks and a descriptive classification for matrix-related mudrock pores. AAPG Bull. 96, 1071–1098. https://doi.org/10.1306/08171111061.

Ma, L., Yu, Q., 2022. Experimental investigation into simultaneous adsorption of water vapor and methane onto shales. J. Hydrol. 604, 127200. https://doi.org/10.1016/j.jhydrol.2021.127200.

Mason, G., 1982. The effect of pore space connectivity on the hysteresis of capillary condensation in adsorption—desorption isotherms. J. Colloid Interface Sci. 88, 36–46. https://doi.org/10.1016/0021-9797(82)90153-9.

Meng, M., Hu, Q., Wang, Q., Hong, Z., Zhang, L., 2024. Effect of initial water saturation and water film on imbibition behavior in tight reservoirs using nuclear magnetic resonance technique. Phys. Fluids 36, 056603. https://doi.org/10.1063/5.0209910.

Newman, A.C.D., 1983. The specific surface of soils determined by water sorption. J. Soil Sci. 34, 23–32. https://doi.org/10.1111/j.1365-2389.1983.tb00809.x.

Niu, J., Zhang, J., Qin, F., Tang, X., Liu, Y., Yuan, T., Tao, J., 2024. Improved calculation method of undervalued free gas in shale: a case study of well Z302 rock in Wufeng-Longmaxi formation, sichuan basin. Energy Fuels 38, 16240–16257. https://doi.org/10.1021/acs.energyfuels.4c02019.

Radliński, A.P., Boreham, C.J., Lindner, P., Randl, O., Wignall, G.D., Hinde, A., Hope, J. M., 2000. Small angle neutron scattering signature of oil generation in artificially and naturally matured hydrocarbon source rocks. Org. Geochem. 31, 1–14. https://doi.org/10.1016/S0146-6380(99)00128-X.

Robin, P.L., Rouxhet, P.G., 1978. Characterization of kerogens and study of their evolution by infrared spectroscopy: carbonyl and carboxyl groups. Geochim. Cosmochim. Acta 42, 1341–1349. https://doi.org/10.1016/0016-7037(78)90039-X.

Ross, D.J.K., Marc Bustin, R., 2009. The importance of shale composition and pore structure upon gas storage potential of shale gas reservoirs. Mar. Petrol. Geol. 26, 916–927. https://doi.org/10.1016/j.marpetgeo.2008.06.004.

Ruppert, L.F., Sakurovs, R., Blach, T.P., He, L., Melnichenko, Y.B., Mildner, D.F.R., Alcantar-Lopez, L., 2013. A USANS/SANS study of the accessibility of pores in the barnett shale to methane and water. Energy Fuels 27, 772–779. https://doi.org/10.1021/ef301859s.

Salmon, E., Behar, F., Hatcher, P.G., 2011. Molecular characterization of Type I kerogen from the Green River Formation using advanced NMR techniques in combination with electrospray ionization/ultrahigh resolution mass spectrometry. Org Geochem. 42, 301–315. https://doi.org/10.1016/j.orggeochem.2010.12.007.

Sang, G., Liu, S., Elsworth, D., 2019. Water vapor sorption properties of illinois shales under dynamic water vapor conditions: experimentation and modeling. Water Resour. Res. 55, 7212–7228. https://doi.org/10.1029/2019WR024992.

Sang, G., Liu, S., Zhang, R., Elsworth, D., He, L., 2018. Nanopore characterization of mine roof shales by SANS, nitrogen adsorption, and mercury intrusion: Impact on water adsorption/retention behavior. Int. J. Coal Geol. 200, 173–185. https://doi.org/10.1016/j.coal.2018.11.009.

Shen, W., Li, X., Cihan, A., Lu, X., Liu, X., 2019. Experimental and numerical simulation of water adsorption and diffusion in shale gas reservoir rocks. Adv. Geo-Energy Res. 3, 165–174. https://doi.org/10.26804/ager.2019.02.06.

Sing, K.S.W., 1985. Reporting physisorption data for gas/solid systems with special reference to the determination of surface area and porosity (Recommendations 1984). Pure Appl. Chem. 57, 603–619. https://doi.org/10.1351/pac198557040603.

Stock, A.T., Littke, R., Schwarzbauer, J., Horsfield, B., Hartkopf-Fröder, C., 2017. Organic geochemistry and petrology of Posidonia Shale (lower Toarcian, Western Europe) – the evolution from immature oil-prone to overmature dry gas-producing kerogen. Int. J. Coal Geol. 176–177, 36–48. https://doi.org/10.1016/j.coal.2017.04.016.

Sun, M., Fu, J., Wang, Q., Gao, Z., 2024. Pore network characterization and fluid occurrence of shale reservoirs: State-of-the-art and future perspectives. Adv. Geo-Energy Res. 12, 161–167. https://doi.org/10.46690/ager.2024.06.01.

Sun, M., Yu, B., Hu, Q., Yang, R., Zhang, Y., Li, B., Melnichenko, Y.B., Cheng, G., 2018. Pore structure characterization of organic-rich Niutitang shale from China: small angle neutron scattering (SANS) study. Int. J. Coal Geol. 186, 115–125. https://doi.org/10.1016/j.coal.2017.12.006.

Sun, M., Zhang, L., Hu, Q., Pan, Z., Yu, B., Sun, L., Bai, L., Connell, L.D., Zhang, Y., Cheng, G., 2019. Pore connectivity and water accessibility in Upper Permian transitional shales, southern China. Mar. Petrol. Geol. 107, 407–422. https://doi.org/10.1016/j.marpetgeo.2019.05.035.

Sun, M., Zhang, L., Hu, Q., Pan, Z., Yu, B., Sun, L., Bai, L., Fu, H., Zhang, Y., Zhang, C., Cheng, G., 2020a. Multiscale connectivity characterization of marine shales in southern China by fluid intrusion, small-angle neutron scattering (SANS), and FIB-SEM. Mar. Petrol. Geol. 112, 104101. https://doi.org/10.1016/j.marpetgeo.2019.104101.

Sun, M., Zhao, J., Pan, Z., Hu, Q., Yu, B., Tan, Y., Sun, L., Bai, L., Wu, C., Blach, T.P., Zhang, Y., Zhang, C., Cheng, G., 2020b. Pore characterization of shales: a review of small angle scattering technique. J. Nat. Gas Sci. Eng. 78, 103294. https://doi.org/10.1016/j.jngse.2020.103294.

Thommes, M., Morell, J., Cychosz, K.A., Fröba, M., 2013. Combining nitrogen, argon, and water adsorption for advanced characterization of ordered mesoporous Carbons (CMKs) and Periodic Mesoporous Organosilicas (PMOs). Langmuir 29, 14893–14902. https://doi.org/10.1021/la402832b.

Tian, X., Duan, X., Sun, M., Mohammadian, E., Hu, Q., Ostadhassan, M., Liu, B., Ke, Y., Pan, Z., 2024. Evolution of fractal characteristics in shales with increasing thermal maturity: evidence from neutron scattering, N_2 physisorption, and FE-SEM imaging. Energy 298, 131342. https://doi.org/10.1016/j.energy.2024.131342.

Tissot, B.P., Welte, D.H., 1984. Petroleum Formation and Occurrence, 2nd, rev.enl. ed ed. Springer-Verlag, Berlin, New York.

Ukaomah, C.F., Sun, M., Pan, Z., Ostadhassan, M., Liu, B., Meng, Q., Aminu, M.D., Fischer, M., 2023. Experimental and molecular investigation of water adsorption controls in marine and lacustrine shale reservoirs. J. Hydrol. 621, 129672. https://doi.org/10.1016/j.jhydrol.2023.129672.

Wang, H., Niu, D., Luan, Z., Dang, H., Pan, X., Sun, P., 2025a. Kinetic characteristics of secondary hydrocarbon generation from oil shale and coal at different maturation stages: insights from open-system pyrolysis. Int. J. Coal Geol. 308, 104845. https://doi.org/10.1016/j.coal.2025.104845.

Wang, L., Du, Y., Wu, G., Fu, X., Xu, C., Pan, Z., 2025b. Application of nuclear magnetic resonance technology in reservoir characterization and CO_2 enhanced recovery for shale oil: a review. Mar. Petrol. Geol. 177, 107353. https://doi.org/10.1016/j.marpetgeo.2025.107353.

Wang, T., Tian, S., Li, G., Sheng, M., Ren, W., Liu, Q., Tan, Y., Zhang, P., 2019. Experimental study of water vapor adsorption behaviors on shale. Fuel 248, 168–177. https://doi.org/10.1016/j.fuel.2019.03.029.

Wang, T., Xu, Z., Yuan, K., Wang, X., Ge, M., 2024. Paleoenvironment and shale gas potential of the Carboniferous Dawuba and the Cambrian Niutitang shales in the Upper Yangtze Platform. South China. Front. Earth Sci. 12. https://doi.org/10.3389/feart.2024.1404178.

Wen, J., Sun, M., Yu, B., Ostadhassan, M., Blach, T.P., Ji, Y., Vu, P., De Campo, L., Wu, C., Mu, J., Ren, Z., Tian, X., Pan, Z., 2024. Risk assessment of high maturity lacustrine shale oil reservoir based on pore-fracture connectivity and decane accessibility, Ordos Basin (China). Mar. Petrol. Geol. 168, 107043. https://doi.org/10.1016/j.marpetgeo.2024.107043.

Wu, Z., He, S., Han, Y., Zhai, G., He, X., Zhou, Z., 2020. Effect of organic matter type and maturity on organic matter pore formation of transitional facies shales: a case study on upper Permian Longtan and Dalong shales in middle Yangtze region. China. J. Earth Sci. 31, 368–384. https://doi.org/10.1007/s12583-019-1237-6.

Xiao, L., Li, Z., Hou, Y., Xu, L., Wang, L., Yang, Y., 2021. Characteristics of organic macerals and their influence on hydrocarbon generation and storage: a case study of continental shale of the Yanchang formation from the ordos basin. China. Geofluids 2021, 5537154. https://doi.org/10.1155/2021/5537154.

Xie, W., Gan, H., Chen, S., Wang, H., Vandeginste, V., Wang, M., 2023. Thermodynamic behavior of water vapor adsorption in shale and its dependence on organic matter and clay minerals. Fuel 352, 129108. https://doi.org/10.1016/j.fuel.2023.129108.

Xing, Y., Xiao, X., Zhao, Y., Liu, W., Fan, Q., Meng, G., Qian, Y., 2025. Thermodynamic and kinetic behaviors of water vapor adsorption on the lower Cambrian over-mature shale and kerogen. Fuel 381, 133560. https://doi.org/10.1016/j.fuel.2024.133560.

Xiong, S., Chen, M., Yu, H., Zhang, W., Hu, Q., He, S., Yang, R., 2023. Experimental investigation of thermodynamic and kinetic behaviors from water vapor adsorption on four typical clay minerals. Gas Sci. Eng. 111, 204933. https://doi.org/10.1016/j.jgsce.2023.204933.

Xu, H., Zhou, W., Hu, Q., Xia, X., Zhang, C., Zhang, H., 2019. Fluid distribution and gas adsorption behaviors in over-mature shales in southern China. Mar. Petrol. Geol. 109, 223–232. https://doi.org/10.1016/j.marpetgeo.2019.05.038.

Xue, Z., Jiang, Z., Wang, X., Gao, Z., Chang, J., Nie, Z., Li, H., Wu, W., Qiu, H., Wang, Q., Hao, M., Chen, R., Liang, Z., 2022. Genetic mechanism of low resistivity in high-mature marine shale: Insights from the study on pore structure and organic matter graphitization. Mar. Petrol. Geol. 144, 105825. https://doi.org/10.1016/j.marpetgeo.2022.105825.

Yang, R., Jia, A., He, S., Hu, Q., Dong, T., Hou, Y., Yan, J., 2020. Water adsorption characteristics of organic-rich Wufeng and Longmaxi Shales, Sichuan Basin (China). J. Pet. Sci. Eng. 193, 107387. https://doi.org/10.1016/j.petrol.2020.107387.

Yang, R., Jia, A., He, S., Hu, Q., Sun, M., Dong, T., Hou, Y., Zhou, S., 2021. Experimental investigation of water vapor adsorption isotherm on gas-producing Longmaxi shale: Mathematical modeling and implication for water distribution in shale reservoirs. Chem. Eng. J. 406, 125982. https://doi.org/10.1016/j.cej.2020.125982.

Zeng, Y., Prasetyo, L., Nguyen, V.T., Horikawa, T., Do, D.D., Nicholson, D., 2015. Characterization of oxygen functional groups on carbon surfaces with water and methanol adsorption. Carbon 81, 447–457. https://doi.org/10.1016/j.carbon.2014.09.077.

Zhang, C., Yao, Y., Swennen, R., Wu, H., 2022. Combined effects of the chemical structure and nanopore development on water vapor/liquid adsorption in shale kerogen. Colloids Surf. Physicochem. Eng. Asp. 653, 129920. https://doi.org/10.1016/j.colsurfa.2022.129920.

Zhang, Y., Jing, X., Jing, K., Chang, L., Bao, W., 2015. Study on the pore structure and oxygen-containing functional groups devoting to the hydrophilic force of dewatered lignite. Appl. Surf. Sci. 324, 90–98. https://doi.org/10.1016/j.apsusc.2014.10.126.

Zhang, Y., Yu, B., Pan, Z., Hou, C., Zuo, Q., Sun, M., 2020. Effect of thermal maturity on shale pore structure: a combined study using extracted organic matter and bulk shale from Sichuan Basin. China. J. Nat. Gas Sci. Eng. 74, 103089. https://doi.org/10.1016/j.jngse.2019.103089.

Zhu, D., Jiang, Z., Jiang, S., Yang, W., Song, Y., Gao, Z., Jiang, T., Cao, X., Li, W., Zhang, Y., 2021. Water-bearing characteristics and their influences on the reservoir capacity in terrestrial shale reservoirs: a case study of the lower Jurassic Ziliujing Formation in the Northeast Sichuan Basin. China. Mar. Petrol. Geol. 123, 104738. https://doi.org/10.1016/j.marpetgeo.2020.104738.

Zolfaghari, A., Dehghanpour, H., Holyk, J., 2017a. Water sorption behaviour of gas shales: I. Role of clays. Int. J. Coal Geol. 179, 130–138. https://doi.org/10.1016/j.coal.2017.05.008.

Zolfaghari, A., Dehghanpour, H., Xu, M., 2017b. Water sorption behaviour of gas shales: II. Pore size distribution. Int. J. Coal Geol. 179, 187–195. https://doi.org/10.1016/j.coal.2017.05.009.